Article

Cell

Nuclear Pores Assemble from Nucleoporin Condensates During Oogenesis

Graphical Abstract

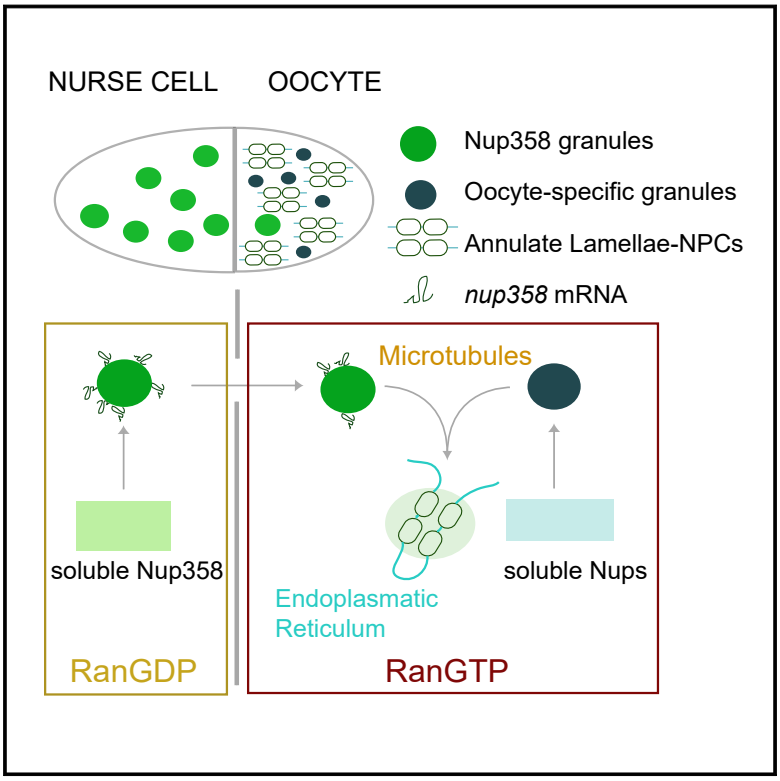

Highlights

- Nucleoporins condense into precursor granules that mature into nuclear pore complexes (NPCs)
- Microtubule-dependent transport and RanGTP promote NPC biogenesis *in vivo*
- *nup358* mRNA localizes to sites of NPC biogenesis in a translation-dependent manner
- Nup358 protein condensation is Ran regulated and controls NPC assembly beyond nuclei

Authors

Bernhard Hampoelz, Andre Schwarz, Paolo Ronchi, ..., Anne Ephrussi, Yannick Schwab, Martin Beck

Correspondence

bernhard.hampoelz@embl.de (B.H.), martin.beck@biophys.mpg.de (M.B.)

In Brief

Nuclear pores form through progressive condensation events during oogenesis

Hampoelz et al., 2019, Cell *179*, 671–686
October 17, 2019
https://doi.org/10.1016/j.cell.2019.09.022

CellPress

Article

Cell

Nuclear Pores Assemble from Nucleoporin Condensates During Oogenesis

Bernhard Hampoelz,[1,2,8,*] Andre Schwarz,[1,3,8] Paolo Ronchi,[4] Helena Bragulat-Teixidor,[4] Christian Tischer,[5] Imre Gaspar,[6] Anne Ephrussi,[6] Yannick Schwab,[4,7] and Martin Beck[1,2,7,9,*]

[1]European Molecular Biology Laboratory, Structural and Computational Biology Unit, Heidelberg, Germany
[2]Max Planck Institute of Biophysics, Frankfurt am Main, Germany
[3]Collaboration for joint PhD degree between EMBL and Heidelberg University, Faculty of Biosciences
[4]European Molecular Biology Laboratory, Electron Microscopy Core Facility, Heidelberg, Germany
[5]Center for Bioimage Analysis, European Molecular Biology Laboratory, Heidelberg, Germany
[6]European Molecular Biology Laboratory, Developmental Biology Unit, Heidelberg, Germany
[7]European Molecular Biology Laboratory, Cell Biology and Biophysics Unit, Heidelberg, Germany
[8]These authors contributed equally
[9]Lead Contact
*Correspondence: bernhard.hampoelz@embl.de (B.H.), martin.beck@biophys.mpg.de (M.B.)
https://doi.org/10.1016/j.cell.2019.09.022

SUMMARY

The molecular events that direct nuclear pore complex (NPC) assembly toward nuclear envelopes have been conceptualized in two pathways that occur during mitosis or interphase, respectively. In gametes and embryonic cells, NPCs also occur within stacked cytoplasmic membrane sheets, termed annulate lamellae (AL), which serve as NPC storage for early development. The mechanism of NPC biogenesis at cytoplasmic membranes remains unknown. Here, we show that during *Drosophila* oogenesis, Nucleoporins condense into different precursor granules that interact and progress into NPCs. Nup358 is a key player that condenses into NPC assembly platforms while its mRNA localizes to their surface in a translation-dependent manner. In concert, Microtubule-dependent transport, the small GTPase Ran and nuclear transport receptors regulate NPC biogenesis in oocytes. We delineate a non-canonical NPC assembly mechanism that relies on Nucleoporin condensates and occurs away from the nucleus under conditions of cell cycle arrest.

INTRODUCTION

Nuclear pore complexes (NPCs) bridge the nuclear envelope (NE) and mediate nucleocytoplasmic exchange. They are giant assemblies of about 110 MDa in animals with an elaborate structure and composition. About 30 different genes encode for NPC components, termed nucleoporins (Nups). Those are subclassified into scaffold Nups that assemble into a cylindrical architecture with a ~50 nm wide central channel; and intrinsically disordered phenylalanine-glycine rich FG-Nups that line this channel. Scaffold Nups assemble into the so-called Y and inner ring complexes that form the outer and inner rings, respectively (Beck and Hurt, 2017; Knockenhauer and Schwartz, 2016). FG-Nups have the capacity to phase separate *in vitro* (Frey et al., 2006; Lemke, 2016). *In vivo*, they establish a unique biophysical milieu within the central channel that is impermeable to inert molecules. FG-Nups transiently interact with nuclear transport receptors (NTRs, also called importins, exportins, or karyopherins) that form complexes with cargo and cross the permeability barrier. Transport directionality across the NE is ensured by the small GTPase Ran. RCC1, the RanGTP exchange factor (RanGEF) is chromatin associated and maintains a high RanGTP concentration in the nucleus. The Ran GTPase activating protein (RanGAP) binds to Nup358 (also called RanBP2) (Forler et al., 2004; Matunis et al., 1998) at the cytoplasmic face of the NPC and ensures high RanGDP levels in the cytosol. Although RanGTP displaces cargo from import complexes in the nucleoplasm, GTP hydrolysis disassembles export complexes once they arrive at the cytoplasmic face (Görlich and Kutay, 1999). Nup358 is absent from lower eukaryotes but essential in animals and involved in active nuclear transport, cell cycle progression, malignant transformation, and viral infection (Campbell and Hope, 2015; Dickmanns et al., 2015; Hoelz et al., 2011; Raices and D'Angelo, 2012).

NPC assembly is an intricate process (Ungricht and Kutay, 2017; Weberruss and Antonin, 2016). In multicellular organisms, two assembly pathways were described (Doucet et al., 2010). First, the relatively rapid assembly of NPCs (Dultz et al., 2008) from pre-existing building blocks concomitantly with nuclear envelope (NE) reformation at the end of open mitosis is referred to as "post-mitotic" assembly. This pathway is spatially directed to chromatin by the Nup Elys (Doucet et al., 2010; Franz et al., 2007; Rasala et al., 2008). Temporal control is provided by cell-cycle-dependent kinases and phosphatases (Ungricht and Kutay, 2017; Weberruss and Antonin, 2016). Second, interphase assembly is a relatively slow process (D'Angelo et al., 2006; Dultz and Ellenberg, 2010) that generates NPCs from scratch in order to double their number for the next mitosis. It proceeds from inside out through the NE (Otsuka et al., 2016) and requires the active nuclear import of Nups (D'Angelo et al., 2006). Here, Nup153 spatially directs the Y complex to the inner nuclear membrane (Vollmer et al., 2015).

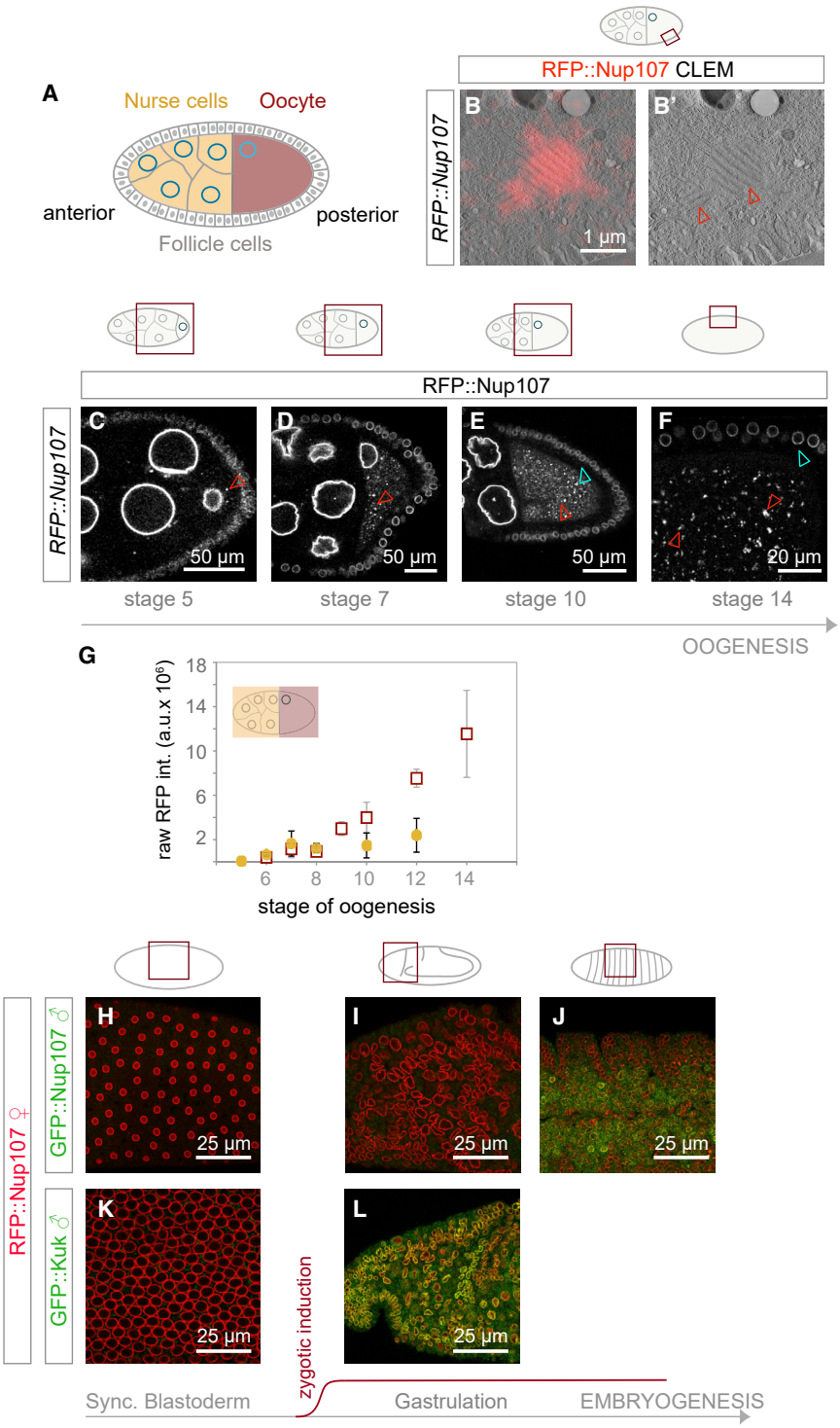

Figure 1. Annulate Lamellae Are Maternally Synthesized

(A) Scheme of the *Drosophila* egg chamber: anterior nurse cells and the posterior oocyte form the germline, both are surrounded by somatic follicle cells. In all further images, anterior is to the left, posterior to the right and an accompanying scheme highlights the image content relative to the egg chamber.

(B and B') RFP::Nup107 enriches at AL-NPCs. Correlative light and electron microscopy (CLEM) of a stage 9 oocyte dissected from a RFP::Nup107 expressing fly. RFP fluorescence concentrates at densely packed NPCs at stacked ER sheets in the oocyte, representing AL (arrowheads in B').

(C–G) AL accumulate during oogenesis. Confocal images of living RFP::Nup107-expressing egg chambers (C–F) during stage 5 (C), 7 (D), 10 (E), and 14 (F). RFP::Nup107-labeled foci accumulate in the cytoplasm of oocytes (red arrowheads in C–F). AL are rare in nurse cells and absent in follicle cells (cyan arrowheads in E and F). In (G) is quantification of raw RFP::Nup107 fluorescence (integrated ± STDV) in either nurse cells (circles) or oocytes (squares) of z projections acquired from images as in (C)–(F) (n = 23 egg chambers). RFP::Nup107 fluorescence stays constant in nurse cells but increases in the ooplasm. Nurse cells have disappeared by stage 14. Abbreviation is as follows: a.u., arbitrary units.

(H–L) Nup107 is maternally contributed. Confocal images from fixed syncytial blastoderm (H and K), gastrulation (I and L) and late stage (J) embryos obtained from RFP::Nup107 mothers fertilized by GFP::Nup107 (H–J) or sqh-GFP::Kuk (K and L) fathers. Nuclei contain only maternal protein prior to zygotic induction (H and K). Nuclei in gastrulation embryos contain zygotic GFP::Kuk (L) but not GFP::Nup107 (I), which is only expressed in later embryo stages (J).

See also Video S1.

Little is known about the early steps of NPC assembly that occur prior to membrane association. FG-Nups serve as a velcro for scaffold Nups (Onischenko et al., 2017). They, however, have a considerable aggregation propensity in isolation (Milles et al., 2013) that has to be controlled during NPC biogenesis *in vivo*. Non-NPC-associated Nups are chaperoned by importin β (Walther et al., 2003). RanGTP dissociates importin β complexes and thereby releases Nups for interphase and post-mitotic NPC assembly (D'Angelo et al., 2006). Likewise, RanGTP induces NPC assembly *in vitro* (Walther et al., 2003), but the *in vivo* relevance of this finding remains to be tested.

In multicellular organisms, nuclear pores also reside in stacked membrane sheets of the endoplasmic reticulum (ER), termed annulate lamellae (AL). Those are particularly prominent in gametes and embryos of a multitude of species (Kessel, 1983) including *Drosophila* (Okada and Waddington, 1959). In early fly embryos, AL insert into the NE in order to supply the rapidly growing nuclei with additional membranes and NPCs (Hampoelz et al., 2016). AL are therefore thought to be maternally provided NPC storage pools. How AL assemble in the absence of a nuclear compartment, which spatially

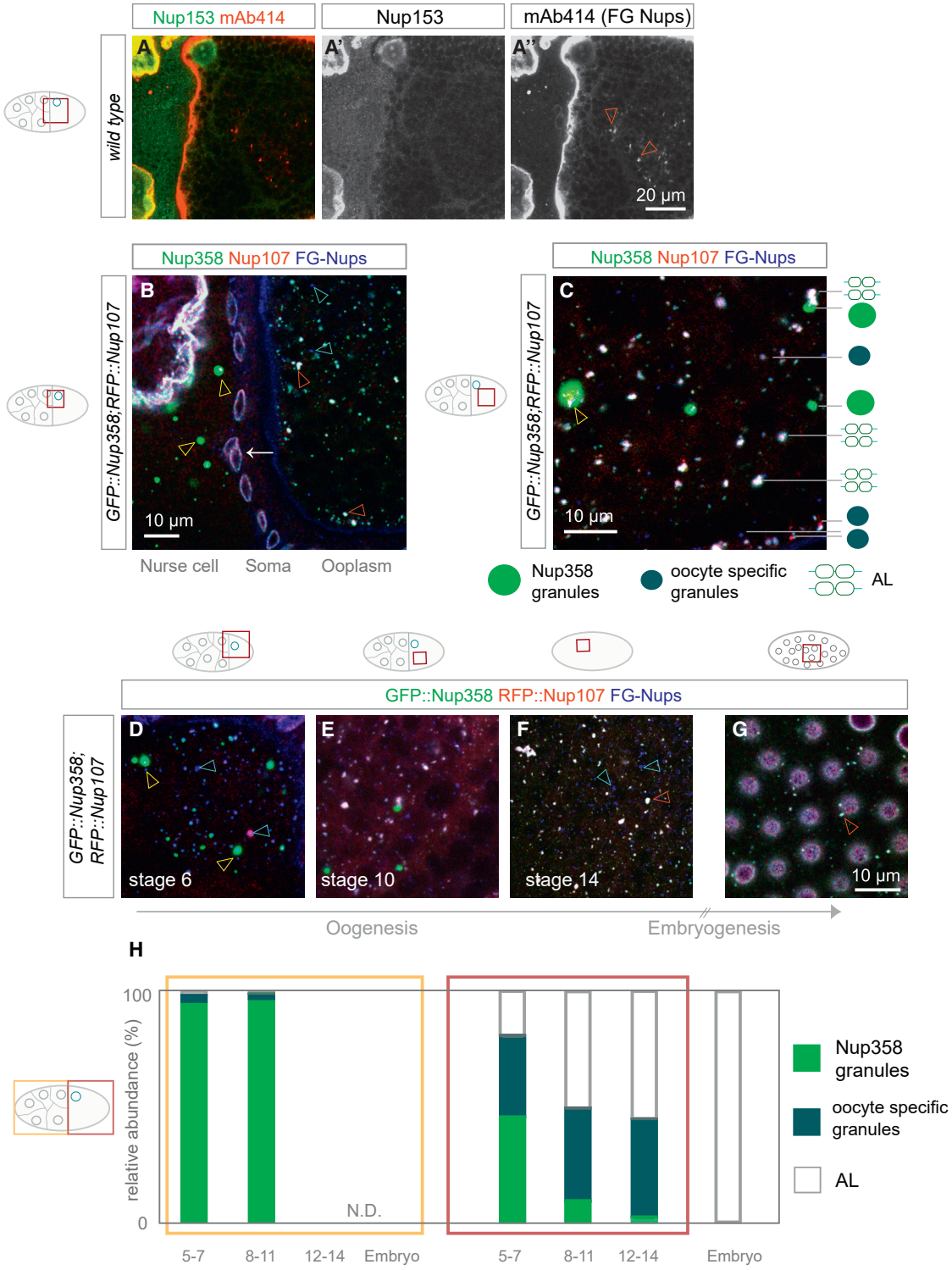

Figure 2. Nups Form Compositionally Diverse Granules

(A) Nup153 does not co-localize with AL. Confocal images (A–A'') from a fixed wild-type stage 10 egg chamber stained with anti-*D.m.* Nup153 (A') and mAb414 recognizing a panel of FG-Nups including Nup358 (A''). Nup153 localizes to the NE and nucleoplasm of nurse cells and the oocyte, but not to mAb414 labeled AL in the ooplasm (red arrowheads in A'').

(B and C) Classes of Nup granules and their spatial distribution during mid-oogenesis. Confocal images from an egg chamber (B) or the ooplasm (C) from fixed ovaries expressing GFP::Nup358 and RFP::Nup107, stained with the FG-Nup marker WGA-Alexa647. (B) Nup358 granules are predominant in nurse cells

(legend continued on next page)

coordinates the process in case of the two previously characterized pathways, remains elusive. Here, we have investigated AL-NPC biogenesis *in vivo* during *Drosophila melanogaster* oogenesis. We found that AL-NPC biogenesis is vastly abundant during oogenesis. It depends on the condensation of Nups into compositionally different granules that are transported along microtubules (MTs) and regulated by Nup358 in concert with Ran and NTRs. We demonstrate that this NPC biogenesis is mechanistically distinct from both canonical NPC assembly pathways and progresses away from chromatin. We propose that instead, Nup358 condensates fulfill the role of spatially directing NPC biogenesis, in the absence of a bona fide nuclear compartment.

RESULTS

Annulate Lamellae Are Maternally Synthesized

In flies the oocyte is specified among a group of sibling cells called nurse cells and matures under conditions of cell cycle arrest to become competent for fertilization (Figure 1A). To test whether AL are synthesized during oogenesis, we used time-resolved fluorescence microscopy and image quantification in transgenic flies expressing the fluorescently labeled scaffold Nup RFP::Nup107. Correlative light and electron microscopy (CLEM) confirmed that RFP::Nup107 located at stacked AL membrane sheets in the ooplasm (Figures 1B and 1B'). Volume imaging with focused ion beam milling coupled to scanning electron microscopy (FIB-SEM) of a stage 10 oocyte detected various AL (Video S1). RFP::Nup107 abundance increased in the ooplasm from stage 5 onward (Figures 1C–1F), whereas it remained somewhat constant at much lower abundance in nurse cells (Figures 1C–1G). There, AL were rare and RFP::Nup107 fluorescence was largely restricted to the NE (Figures 1C–1E). The surrounding somatic cells were devoid of AL (Figures 1E and 1F).

To confirm that this maternal pool of AL is indeed used during embryogenesis, we crossed females expressing RFP::Nup107 to males expressing either GFP::Nup107 or GFP::Kugelkern (Kuk), a known zygotic NE component as control (Brandt et al., 2006). GFP::Nup107 stayed absent from nuclei not only throughout syncytial blastoderm stages but, in contrast to the zygotically induced GFP::Kuk, also at gastrulation and got incorporated into nuclei only in late-stage embryos (Figure 1H–1L). We conclude that AL accumulate specifically in oocytes in order to provide storage for early embryogenesis.

Nups Form Compositionally Diverse Granules

In embryonic AL-NPCs, most peripheral Nup subcomplexes are missing (Hampoelz et al., 2016). A notable exception is Nup358 that localizes to AL-NPCs but its functional relevance remains unclear. Although we detected Nup153 at the NE in the egg chamber, it was absent from AL (Figures 2A–2A''). This is in line with AL-NPC composition in the embryo (Hampoelz et al., 2016) and suggests that AL-NPC biogenesis is distinct from interphase NPC assembly that requires Nup153 (Vollmer et al., 2015). To visualize Nup358 localization, we generated transgenic flies expressing an N-terminal emeraldGFP Nup358 fusion protein (GFP::Nup358) by using a CRISPR/Cas9 induced knock-in into the endogenous locus. GFP::Nup358 localized to the NE and to AL as expected (Figures S1A, S1A'', and 2B) and in both cases co-localized with RFP::Nup107 (Figure 2B and 2C) and the FG-Nup marker wheat germ agglutinin (WGA) (Figures S1A–S1A'', 2B, and 2C), indicative of fully assembled NPCs. Triple-positive AL are variable in size and restricted to oocytes (Figure 2B and 2C). Strikingly, there were also two other types of granules, which were distinct from AL: (1) perfectly spherical, Nup358-positive granules are larger and brighter than AL (Figures S1A, S1A', 2B, and 2C). The vast majority of their volume is Nup107- and FG-Nup-negative but they might contain scaffold and FG-Nups in confined regions (yellow arrowhead in Figure 2C). These "Nup358 granules" are prevalent in nurse cells and only occasionally observed in the oocyte. (2) In oocytes, we also observed smaller granules that were negative for Nup358 (Figures 2B and 2C). They stained for either Nup107 or FG-Nups or both (Figures 2B and 2C). We will refer to them as "oocyte-specific granules." Granules were not due to overexpression: GFP::Nup358 replaces endogenous Nup358 and RFP::Nup107 condensation was unchanged in egg chambers from females where the RFP fusion protein rescues a null allele of *nup107* (Figures S1B–S1C'') (Katsani et al., 2008). We quantified the spatiotemporal distribution of AL and both classes of granules and found that Nup358 granules diminish toward later stages of oogenesis (Figure 2D–2H), whereas oocyte-specific Nup granules persist until very late oogenesis (Figure 2F and 2H). AL accumulate progressively during oogenesis (Figures 1G, and 2D–2H) and in contrast to both classes are also observed in blastoderm embryos (Figures 2G and 2H).

MT-Dependent Transport Promotes Nup Granule Interactions

On the basis of the spatial and temporal abundance distribution of the different granules, we hypothesized that granules of both

(yellow arrowheads) whereas oocyte-specific granules (cyan arrowheads) and triple-labeled AL (red arrowheads) populate the oocyte. Nup granules of both classes are absent from somatic follicle cells (white arrow). All three markers localize at the NE of nurse and follicle cells. In (C) is the classification of Nup granules in the oocyte. Nup358 granules are GFP::Nup358 positive and spherical and can contain other Nups in confined regions (yellow arrowhead). Oocyte-specific granules can contain one or two Nup markers. Mature AL-NPCs are triple positive.

(D–H) Temporal distribution of Nup granules in fixed oocytes (D–F) and a syncytial blastoderm embryo (G) expressing GFP::Nup358 and RFP::Nup107, stained with WGA-Alexa647. In (H) is the quantification of granule distribution during development. Nup358 granules, oocyte-specific granules, and AL were counted on 5 μm spanning z-projections from fixed samples as in (D)–(G). The percentage of each class is represented for early (stages 5–7), mid (stages 8–11), late (stages 12–14) oogenesis egg chambers and embryos. In nurse cells, Nup358 granules (yellow arrowheads in D) dominate during early and mid-oogenesis. Nurse cells degrade in late-stage egg chambers (N.D.). In oocytes, the number of Nup358 granules decreases during oogenesis, whereas the number of oocyte-specific granules (cyan arrowheads in D and F) stays constant. The number of AL (red arrowheads in F and G) increases, and in contrast to both classes, AL are present in embryos. Number of quantified egg chambers is as follows: n = 6 (early oogenesis), n = 5 (mid oogenesis), n = 4 (late oogenesis).

See also Figure S1.

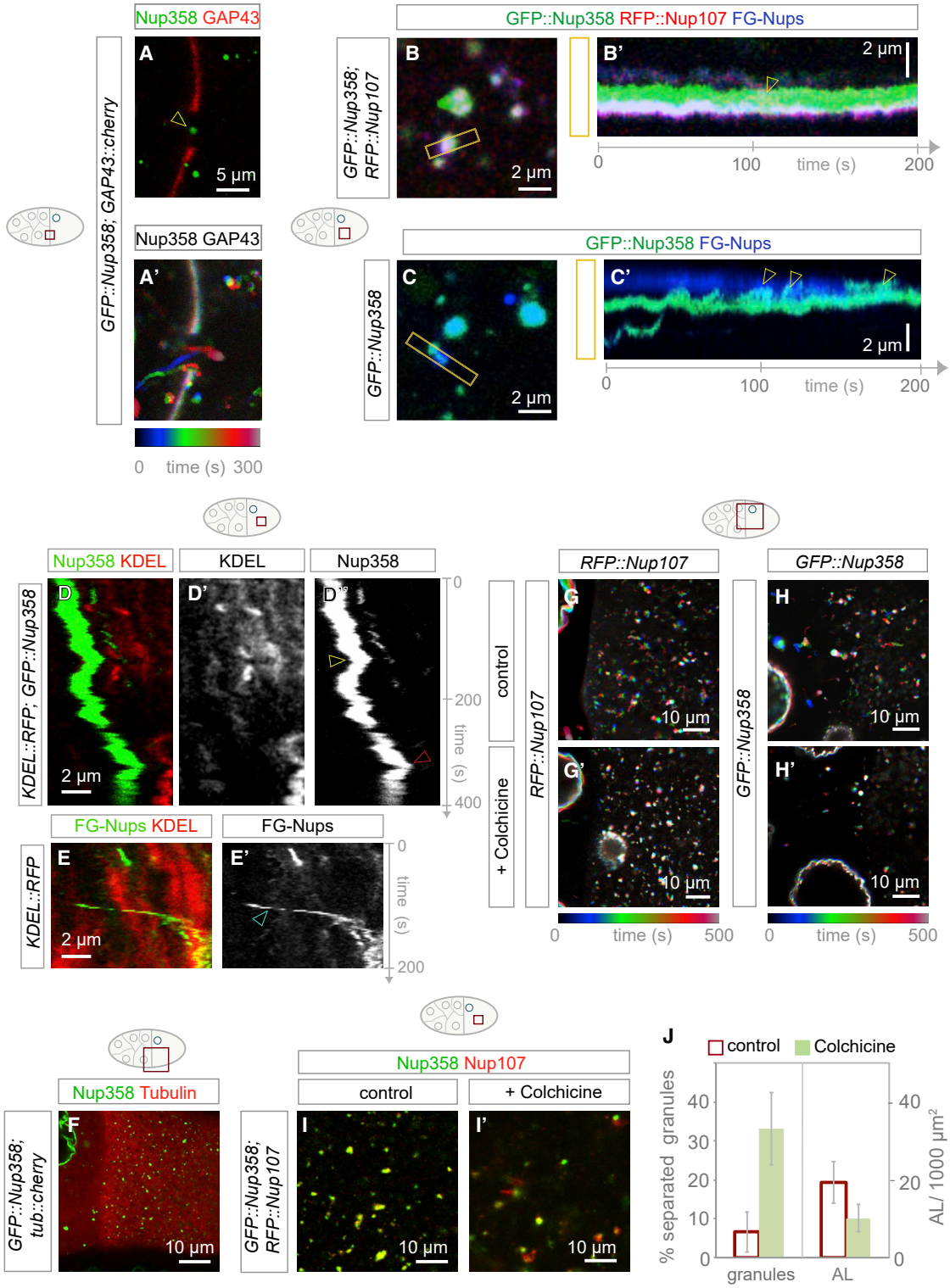

Figure 3. Microtubule-Dependent Transport Promotes Nup Granule Interactions

(A) Nup358 granules migrate from nurse cells to the ooplasm. Shown are a top view image (A) and color-coded time projection (A') of a video taken of an egg chamber expressing GFP::Nup358 and the plasma membrane marker GAP43::cherry. Nup358 granules move into the oocyte through a ring canal (arrowhead in A), signified by the gap in the GAP43::cherry staining.

(legend continued on next page)

classes are NPC precursors that progress into AL in oocytes (Figure 2H). Consistent with this concept, Nup358 granules traveled from nurse cells into the ooplasm through ring canals that connect the cytoplasm across nurse cells and the oocyte (Figures 3A and 3A'; Video S2). To investigate the fate of oocyte specific granules, we recorded and quantified videos of living egg chambers (n = 4; time frame 16–47 min; representative data shown as Video S3). Most oocyte-specific granules (n = 21) were engaged in direct contact with either Nup358 granules (Figures 3B and 3B'; Video S3) or AL (Figure 3C and 3C'; Video S3), allowing the transfer of material (Figures 3B' and 3C'). Granules formed contacts on average timescales that are much shorter (~10 min) than overall AL biogenesis. Granules were dynamic and movements were often independent from membranes (Figure 3D–3E'). These findings further suggest that granules of both classes are NPC precursors. They can form prior to membrane association and interact, presumably to exchange Nups for AL-NPC assembly.

Live imaging of FG-Nups in the oocyte revealed two kinds of motion. First, they showed locally restricted fluctuations, presumably generated by ER dynamics in case of AL (Waterman-Storer and Salmon, 1998) (Figure 3D''; Videos S3 and S4). Second, they displayed fast and directed runs indicative of motor-dependent transport along MTs (arrowhead in Figure 3E'; Video S4). GFP::Nup358 granules localized to MTs in intact egg chambers (Figure 3F) and did undergo directed runs along MT fibers in *ex vivo* squash preparations (Video S5). All of these motions were dependent on intact MTs: Colchicine feeding inhibited the dynamics of RFP::Nup107- and GFP::Nup358-labeled granules (Figure 3G'–3H'; Video S4). Although granules of both classes persisted colchicine treatment, they often remained separated and did not mix with each other (Figures 3I, 3I', and 3J). This resulted in less AL (Figure 3J) and suggests that MT-dependent transport enforces granule interactions, which is essential to form AL-NPCs.

Nup Granules Fulfill Hallmarks of Biomolecular Condensates

Most granules were perfectly spherical (Figures 2B, 2C, S1D-S1D''', and 4A-A'''). Upon direct contact they established an interface indicative of surface tension between droplets with controlled miscibility (Figure S1D–S1D''', 4B–4B''; Video S3). Imaging of multi-labeled ovaries confirmed the existence of small, yet confined sub-structures within Nup358 granules that were populated by other Nups including Nup107, Nup214, FG-Nups, and surprisingly, the transmembrane Nup gp210 (Figures 2C, 4A-4A''', and S1D–S1E''). This layered droplet behavior is indicative of granules with different chemical potentials encoded in their sequence. It agrees with recent work that reported differential co-condensation of purified intrinsically disordered regions from multiple Nups (Konishi and Yoshimura, 2019).

The hydrophobic interactions stabilizing many phase separated condensates and the permeability barrier of the NPC formed by FG-Nups are sensitive to treatment with 1,6-hexanediol (Ribbeck and Görlich, 2002). Incubation of dissected ovaries with 5% 1,6-hexanediol generally interfered with the integrity of granules of both classes as well as mature pores at AL and at the NE (Figures S2A–S2B'''). Fluorescence recovery after photobleaching (FRAP) experiments indicated relatively fast exchange of material within granules (Figures S2C–S2C''). Dual-color CLEM experiments revealed that in nurse cells, RFP::Nup107 was either absent from Nup358 granules or decorated a small membrane associated portion, whereas GFP::Nup358 itself filled a large round zone entirely devoid of ribosomes, indicating a different biophysical milieu as compared with the surrounding ribosome-dense cytoplasm (Figures 4C and 4C').

In the oocyte, Nup358 granules contained various degrees of membrane sheets and scaffold Nups, presumably comprising intermediate stages of AL assembly (Figure 4D–4F'). Volume imaging confirmed that AL were never fully surrounded by ER membranes (Figures S2D–S2D''; Video S6) and thus accessible to the cytosol. Nevertheless, AL maintained an intrinsic and proximal "ribosome exclusion zone" (Figures 4F and 4F') that was also observed in single-sheeted AL (Figure S2E), but not at the ER, where ribosomes were immediately adjacent to membranes (Figures 4F' and S2E). In CLEM experiments the ribosome-free zone appeared Nup358 positive (Figure 4F), indicative of a specific local milieu that is common to both Nup358 granules and AL. Condensation was not due to the GFP tag, as we observed similar ribosome exclusion zones in egg chambers that expressed wild type Nup358 (Figures S2F and S2F').

(B and C) Interactions between Nup granules and AL. Shown are stills (B and C) or kymographs (B' and C') from videos capturing GFP::Nup358 and RFP::Nup107 (B and B') or GFP::Nup358 (C, and C') expressing egg chambers, injected with the FG-Nup marker WGA-Alexa647. Kymographs were produced from the boxed regions indicated in (B and C). Shown and (B and B') is interaction between a Nup358 granules and a RFP::Nup107/FG-Nup-positive, oocyte-specific granule. Shown in (B'), granules stay adjacent with little overlap and controlled material transfer (arrowhead). Shown in (C') is a representative event of an interaction between a FG-Nup-labeled, oocyte-specific granule and an AL with mixing (arrowheads).

(D and E) Nup granules can occur independent of ER membrane. Kymographs (D–E') obtained from movies recording a representative stage 10 nurse cell (D–D'') or oocyte (E and E') dissected from flies expressing either GFP::Nup358 and the ER marker KDEL::RFP (D–D'') or KDEL::RFP, injected with WGA-Alexa488 labeling FG-Nups (E and E'). Shown in (D–D''), KDEL::RFP temporally co-localizes with a GFP::Nup358 (yellow arrowhead in D''), before KDEL::RFP loses contact from the Nup358 granule. Shown in (E and E'), a FG-Nup-labeled, oocyte-specific granule undergoes a fast directed run independent of KDEL::RFP (cyan arrowhead in E'), before it attaches to membrane.

(F–J) Microtubules are crucial for granule dynamics and mixing. Shown in (F) is a confocal image from a video recorded in ovaries expressing GFP::Nup358 and Tubulin::cherry. Nup358 granules localize to the dense MT network. Shown in (G and H) are color-coded temporal projections (G–H') or stills (I and I') of a video recording control (G, H, and I) or Colchicine-treated (G', H', and I') egg chambers that express RFP::Nup107 (G and G'), GFP::Nup358 (H and H'), or both (I and I'). Colchicine treatment reduced NPC precursor granule and AL dynamics (G' and H'), compared with controls (G and H), and impaired granule mixing (I') compared with controls (I). Shown in (J) is the quantification of granule separation and AL number in Colchicin-treated (n = 10 egg chambers) and control (n = 8) mid-oogenesis egg chambers: MT de-polymerization increases the percentage of separated GFP::Nup358 and RFP::Nup107 granules and reduces AL number. Data represent means ± STDV.

See also Videos S2, S3, S4, and S5.

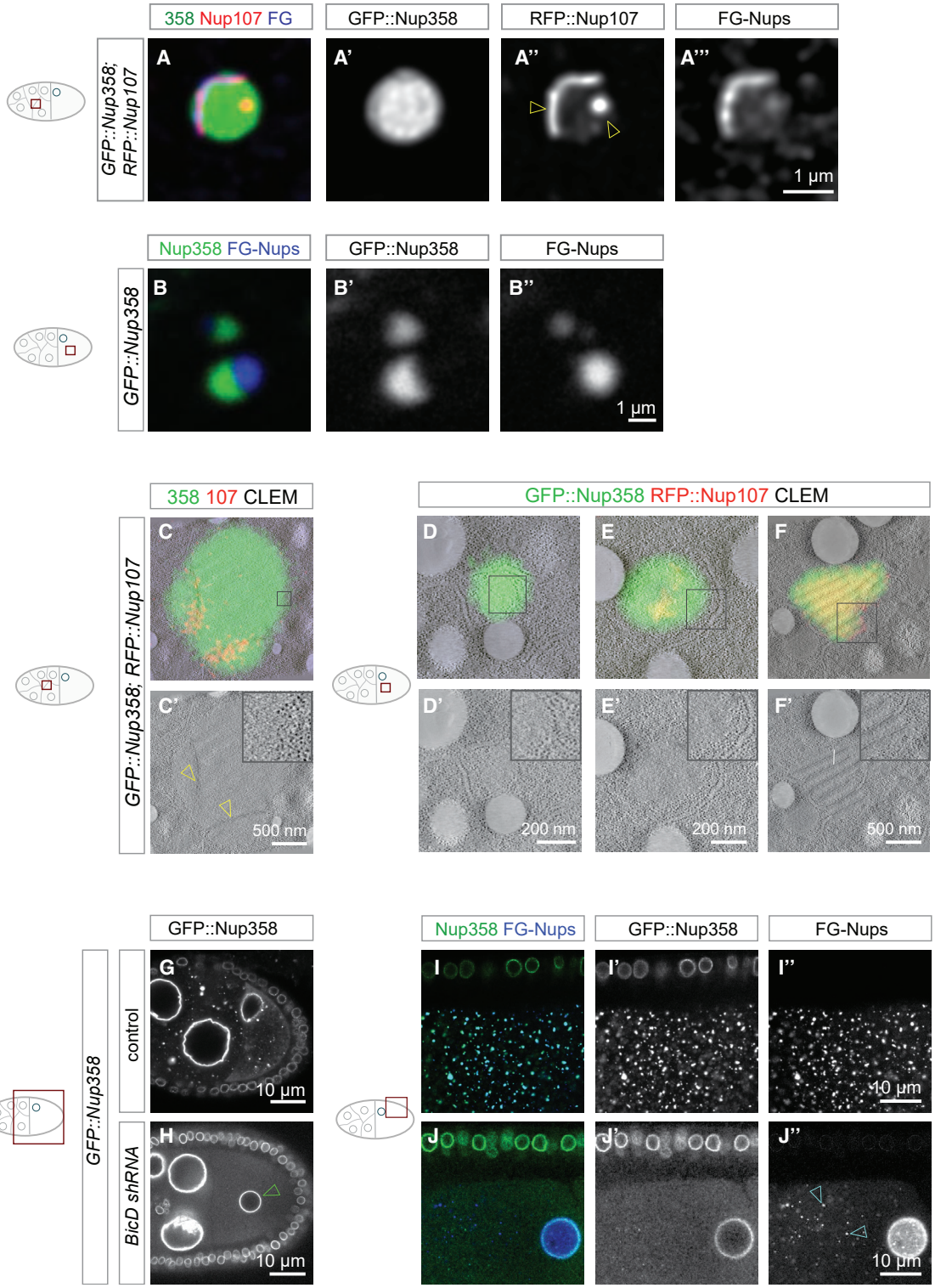

Figure 4. Nup358 Condensates Are Required for AL-NPC Biogenesis

(A and B) NPC granules resemble condensates with limited miscibility. De-convolved confocal image of a fixed nurse cell cytoplasm (A–A''') or ooplasm (B–B'') from flies expressing GFP::Nup358 and RFP::Nup107 (A) or GFP::Nup358 (B), and stained with WGA-Alexa647 to label FG-Nups. Within a spherical Nup358 granule (A') RFP::Nup107 (A'') and FG Nups (A''') demark specific subregions without mixing (arrowheads in A''). Shown in (B–B''), despite a large contact area, Nup358 granules and FG-Nup-labeled, oocyte-specific granules do not instantaneously mix.

(legend continued on next page)

Nup358 Condensates Are Required for AL-NPC Biogenesis

Our findings suggest that Nup358 could be critical for the assembly of non-nuclear NPCs. Consistent with its essential role in mouse embryogenesis (Dawlaty et al., 2008), shRNA-mediated gene silencing of Nup358 abolished embryonic development in flies, although efficient depletion was only achieved from mid-oogenesis onward (Figures S3A–S3D), potentially masking earlier requirements for the Nup358 protein in forming AL. However, in later stage egg chambers, loss of Nup358 did not only abolish Nup358 granules, it also reduced AL number and impaired their organization (Figure S3E–SG''). Residual AL clustered into large aberrant assemblies, whereas patches devoid of Nup358 formed elongated structures instead of compact shapes (Figure S3F–S3G''). CLEM experiments in Nup358-depleted ovaries revealed RFP::Nup107-labeled, yet NPC-free patches with partially disturbed ribosome exclusion zone (Figure S3H and S3H'). We cannot formerly distinguish whether these structures derived from disintegrating pre-existing AL or whether they represent oocyte-specific granules incapable to progress into AL due to the lack of Nup358 granules. We conclude that Nup358 facilitates assembly of AL into compact structures with multiple stacked membrane sheets.

Nup358 granules are transported along MTs (Video S5) and could be linked to motors by the adaptor protein BicD that binds Nup358 in mammalian cells (Splinter et al., 2010). In flies, BicD is involved in oocyte specification and polarity (Mach and Lehmann, 1997). shRNA-mediated knockdown of *BicD* (Figures S3I and S3I') resulted in sterility and egg chambers with previously described phenotypes indicative of compromised BicD activity (Suter et al., 1989; Swan and Suter, 1996). Under these conditions, GFP::Nup358 was still present at the NE but failed to form granules and appeared largely soluble (Figure 4H). No AL formed in the ooplasm (Figures 4J–J'') despite the existence of FG-Nup-positive, oocyte-specific granules (Figure 4J''). Although we cannot mechanistically explain how BicD controls Nup358 granule formation, these findings indicate that not the presence of Nup358 per se, but its condensation into granules is important for AL biogenesis.

nup358, *nup153*, and *importin β* mRNAs Localize to Sites of NPC Biogenesis in a Translation-Dependent Manner

In analogy to the polarization of the fly oocyte (St Johnston, 2005), the observed asymmetric Nup granule distribution could derive from localized translation of the respective mRNAs. We systematically screened the localization of Nup and NTR encoding mRNAs using single-molecule fluorescence *in situ* hybridization experiments (smFISH) (Raj et al., 2008) (Figures S4A–S4A'' and S4B). Most of these mRNAs were dispersed throughout the egg chamber and oogenesis (Figures S4C–S4D'' and S5), with the exception of *ndc-1* concentrating at the ER (Figures S4E–E'') and *nup160, rcc-1*, and a few NTR-encoding mRNAs that were enriched in early oocytes (Figure S5).

Out of 39 tested mRNAs, namely *nup358*, *nup153*, *ketel* (*importin β1*), *karyopherin β3* (*importin β5*), and *moleskin* (*importin β7*), five were enriched at the surface of AL, the NE, and Nup358 granules as compared with controls (Figure 5A–5D and S4F–S4H'). Except *ketel,* these transcripts were more enriched at Nup358 granules in nurse cells than at mature AL in oocytes (Figure 5D). Strikingly, within AL-granule interaction zones, the *nup358* mRNA was absent in areas that stained exclusively for FG-Nups (Figure 5E–5E'''). Unlike *oskar,* which lost its localization to the posterior oocyte pole as previously reported (Clark et al., 1994), *nup358* and *ketel* remained enriched along AL upon treatment with the MT depolymerizing drug Colchicine (Figures 5F and 5G).

Puromycin treatment disrupts polysomes and entirely abolished the enrichment of *nup358 and ketel transcripts* at AL or the NE, whereas posterior *oskar* enrichment was not affected (Figures 5H and 5I). In contrast, cycloheximide, which arrests translation by freezing nascent chain elongation, preserved mRNA localization (Figures 5J and 5K). Ribosome run off triggered by the translation initiation inhibitor homoharringtonine revealed that mRNA localization correlated with transcript length (Figure S4I–S4I'''). This progressive loss of enrichment was abolished by simultaneous block of elongation using cycloheximide (Figures S4I–S4I''). Our results indicate that the respective mRNAs localize to sites of NE-NPC or AL-NPC biogenesis only when a nascent peptide chain is present, different from axis determinants like *oskar* that are translationally repressed until they reach their destination through MT-dependent transport (St Johnston, 2005). We conclude that translation-dependent mRNA enrichment might contribute to effective condensation of Nups but cannot explain asymmetric granule occurrence.

(C) Nup358 granules are sites of NPC biogenesis. Shown in (C and C'), is a dual-color CLEM of a nurse cell Nup358 granule that contains RFP::Nup107 in confined subregions with membrane (arrowheads in C'). GFP::Nup358 fills a large sphere that in Transmission EM (C') appears devoid of ribosomes, compared with the surrounding cytoplasm. The condensate border is magnified in the inset in (C'); the rectangle in C represents the inset area.

(D–F) Stages of AL biogenesis. Shown are dual-color CLEM images acquired in stage 9 oocyte of a high-pressure frozen egg chamber expressing GFP::Nup358 and RFP::Nup107. GFP::Nup358 labels spherical ribosome free condensates without RFP::Nup107 and membrane (D and D') or with a portion decorated with RFP::Nup107 (E and E'). Mature AL (F and F'), signified by multiple RFP::Nup107-labeled pores along stacked ER membranes maintain a GFP::Nup358 halo surrounding the AL. GFP::Nup358-positive regions between the membranes and adjacent to the outermost sheets maintain a ribosome exclusion zone. The respective condensate borders are magnified in the insets in (D', E', and F'); rectangles in (D, F, and G) represent the magnified ROIs.

(G–J) Nup358 condensates are required for AL-NPC assembly. Shown in (G)–(H) are stills from a video imaging mid-oogenesis control (G) or *BicD-shRNA*-induced (H) egg chambers expressing GFP::Nup358. GFP::Nup358 localizes to the NE but in contrast to controls (G) does not condense but is soluble upon BicD depletion (H). The mis-localized oocyte nucleus in the interior of the ooplasm in *BicD*-shRNA-treated ovaries is indicative of compromised BicD activity (green arrowhead in H). Shown in (I)–(J'') are confocal images from fixed late stage control (I–I'') or *BicD-shRNA*-induced (J–J'') egg chambers expressing GFP::Nup358 stained with WGA-Alexa647 to label FG Nups. FG-Nups form oocyte specific granules (arrowheads in J'') but do not assemble double-labeled AL upon BicD depletion as compared with control oocytes (I).

See also Figures S2 and S3 and Video S6.

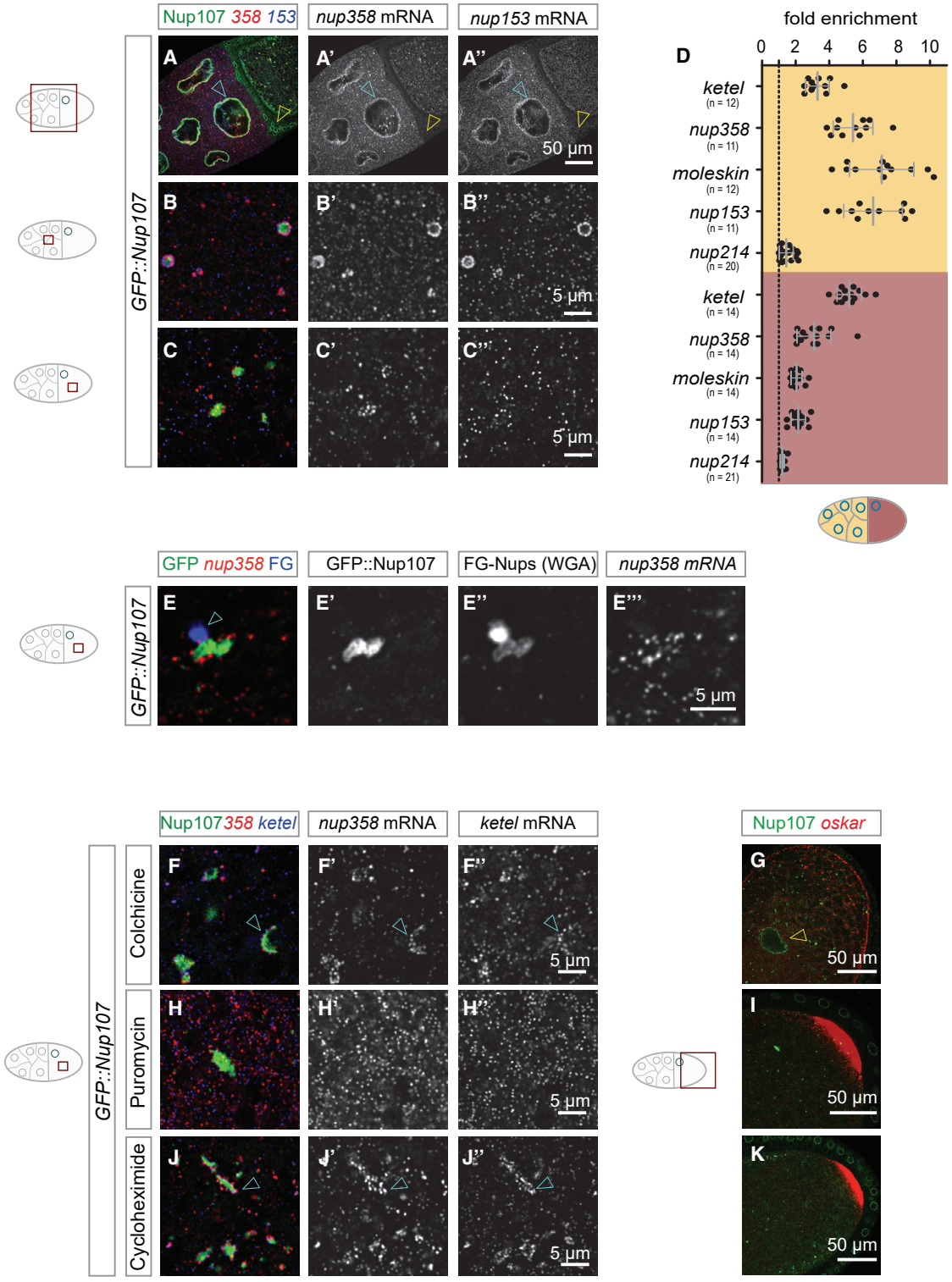

Figure 5. A Specific Subset of NTR and Nup Encoding mRNAs Enrich at Sites of NPC Biogenesis

(A–D) *nup358*, *nup153*, and specific NTR transcripts are enriched at Nup358 granules and AL. Shown in (A)–(C'') are top views of fixed GFP::Nup107-expressing egg chambers (A–A''), nurse cell cytoplasm (B–B''), or ooplasm (C–C''), hybridized with smFISH probes detecting *nup358* and *nup153*, respectively. *nup358* (A and A') and *nup153* (A and A'') mRNAs localize at the NE in nurse cells (blue arrowheads) but not in follicle cells (yellow arrowheads). *nup358* transcripts surround Nup358 granules in nurse cells (B and B') and AL in oocytes (C and C'), and *nup153* mRNA enriches in nurse cell precursors (B and B'') but not in oocytes

(legend continued on next page)

Ran and Crm1 Spatially Control Nup Condensation and AL Assembly

Ran plays an important role in both canonical NPC assembly pathways (D'Angelo et al., 2006; Walther et al., 2003). We therefore wanted to test whether it directs AL biogenesis toward the oocyte. Nup358 interplays with Ran activity by recruiting RanGAP to the cytoplasmic face of NE-NPCs. Consistently, RanGAP perfectly co-localized with Nup358 not only at the NE but also to previously reported (Cesario and McKim, 2011) yet uncharacterized germline specific cytoplasmic foci, revealing them as AL or Nup358 granules (Figures S6A–6A'''). Nup358 gene silencing largely abolished RanGAP localization to NPCs as well as Nup358 granules and released it to the cytoplasm (Figures S6B–6B'''). Interestingly, both GFP::Nup358 and RanGAP displayed a much brighter fluorescence in Nup358 granules than AL or the NE, indicating Nup358 dilution upon progression into AL (Figures S6C–S6E'). RanGAP was enriched at the NE of nurse cells as compared with the oocyte nucleus (Figure 6A and 6A'). Consistent with earlier reports (Frasch, 1991), RCC1 was strongly enriched in the oocyte nucleus compared with nurse cells (Figure 6A''). Moreover, although undetectable in the cytoplasm of nurse cells, RCC1 levels were elevated in the ooplasm (Figure 6B''). These data support the notion that the milieu of the oocyte is different from nurse cells, thus spatially directing AL biogenesis. They support the existence of an elevated ooplasmic pool of RanGTP *in vivo*, as previously suggested (Ryan et al., 2003; D'Angelo et al., 2006).

We thus directly addressed whether the nucleotide status of Ran affects AL-NPC assembly *in vivo*. We overexpressed *Drosophila* wild-type Ran or the Ran mutants T24N or Q69L that lock either the GDP or GTP bound state, respectively (Cesario and McKim, 2011; Klebe et al., 1995). RanT24N expression reduced both AL and Nup358 condensates (Figures 6C and 6E–6E''') compared with wild-type Ran (Figure 6C–6D'''). In contrast, RanQ69L, which strongly co-localized with Nup358 (Figures 6F–6F'') (Cesario and McKim, 2011) stimulated Nup358 condensation in nurse cells (Figures 6C and 6F–6F'). It also induced AL agglomeration in the ooplasm with a local enrichment at the anterior border, but not in nurse cells (Figure 6F–6F'''). Given that MT-dependent transport promotes AL biogenesis (Figure 3J), we tested whether de-polymerization of MTs can revert RanQ69L-induced AL agglomerates, which was indeed the case (Figures S6F and S6F').

This agrees with previous work showing that Ran controls NTR-mediated chaperoning of non-NPC-associated Nups *in vitro* and promotes NPC biogenesis (Walther et al., 2003). Conceptually extending this model, Ran-regulated NTR chaperoning could spatially control Nup condensation *in vivo*, as a prerequisite for AL biogenesis. We experimentally tested this for both importins and exportins. Althought the results were not clear for *ketel* (not shown), presumably due to the redundancy of importins, depletion of the *Drosophila crm1* homolog *embargoed* abolished GFP::Nup358 condensation in nurse cells and rendered the protein largely soluble (in 60% of the observed egg chambers; n = 17) (Figures 6G, 6H, and S6G). In 40% of the egg chambers, the spatial organization of Nup condensation was inverted. Specifically, Nup358 granules appeared in oocytes instead of nurse cells and very rarely oocyte-specific granules appeared in nurse cells (Figure 6I–6J''). Importantly, AL assembly was suppressed under these conditions, underlining the importance of correctly compartmentalized Nup condensation (Figure 6I–6J''). How exactly the different NTRs distribute between nurse cells and oocyte and which specifically chaperone the individual Nups, remains to be further investigated.

DISCUSSION

A Model for NPC Biogenesis Beyond the Nuclear Compartment

Little was known about the biogenesis of AL and the spatial cues that allow NPC formation away from the nuclear compartment. Our work addresses these questions during *Drosophila* oogenesis and suggests a third, non-canonical NPC assembly mechanism. Already in nurse cells, Nup358 condenses into large granules (Figures 7A and 7B). Condensation might be fostered by local translation of *nup358* transcripts that enrich at the surface of Nup358 granules in a translation dependent manner (Figure 7B). In nurse cells, AL biogenesis is suppressed, and only limited NPC assembly is observed within Nup358 granules (Figure 7B). This could be due to the available amount or configuration of ER membranes (Röper, 2007) or because high cytoplasmic concentrations of RanGDP promote the formation of Importin-Nup complexes that prevent other Nups from condensation (Figure 7B) (Walther et al., 2003). Nup358 granules become assembly platforms for AL-NPCs once they travel through ring canals into the ooplasm. Scaffold and FG-Nups condense into oocyte specific granules, possibly facilitated by elevated levels of RanGTP that dissociates the respective Nups from Importin (Walther et al., 2003) (Figure 7B'). In the oocyte, NPC precursor granule interactions are promoted by

(C and C''). Shown in (D) is the quantification of mRNA enrichment around Nup358 granules or AL relative to the average cytoplasmic intensity. *nup214* mRNA serves as non-localized control. All quantified mRNAs except *ketel* are more enriched at Nup358 granules in nurse cells compared with AL in oocytes. N corresponds to subvolumes in respective regions of egg chambers. Bars represent mean ± STDV.

(E–E''') *nup358* transcripts do not enrich at FG-Nup-labeled, oocyte-specific granules. Top views on AL in the ooplasm from fixed GFP::Nup107-expressing ovaries, labeled with WGA-Alexa647 and hybridized with smFISH probes detecting *nup358* mRNA. *nup358* transcripts are excluded from the attaching FG-Nup-labeled, oocyte-specific granule. The images are z-projections over 500 nm.

(F–K) *nup358* and *ketel* enrichment is translation dependent. Top view images from the ooplasm (F–J'') or the posterior region of oocytes (G, I, and K) of fixed ovaries expressing GFP::Nup107, treated with either colchicine (F–F'' and G), puromycin (H–H'' and I), or cycloheximide (J–J'' and K). *nup358* and *ketel* enrichment at GFP::Nup107 is not affected by colchicine (F–F''), which effectively depolymerizes MTs as indicated by the mis-positioned oocyte nucleus (arrowhead in G) and failed posterior accumulation of *oskar* mRNA (G). Puromycin abolishes enrichment of *nup358* (H and H') and *ketel* (H and H'') at GFP::Nup107-labeled AL but not of *oskar* at the posterior oocyte pole (I). Cycloheximide does neither interfere with *nup358* (J and J'), nor with *ketel* (J and J'') transcript enrichment at AL. It does also not impair posterior accumulation of *oskar* (K).

See also Figures S4 and S5.

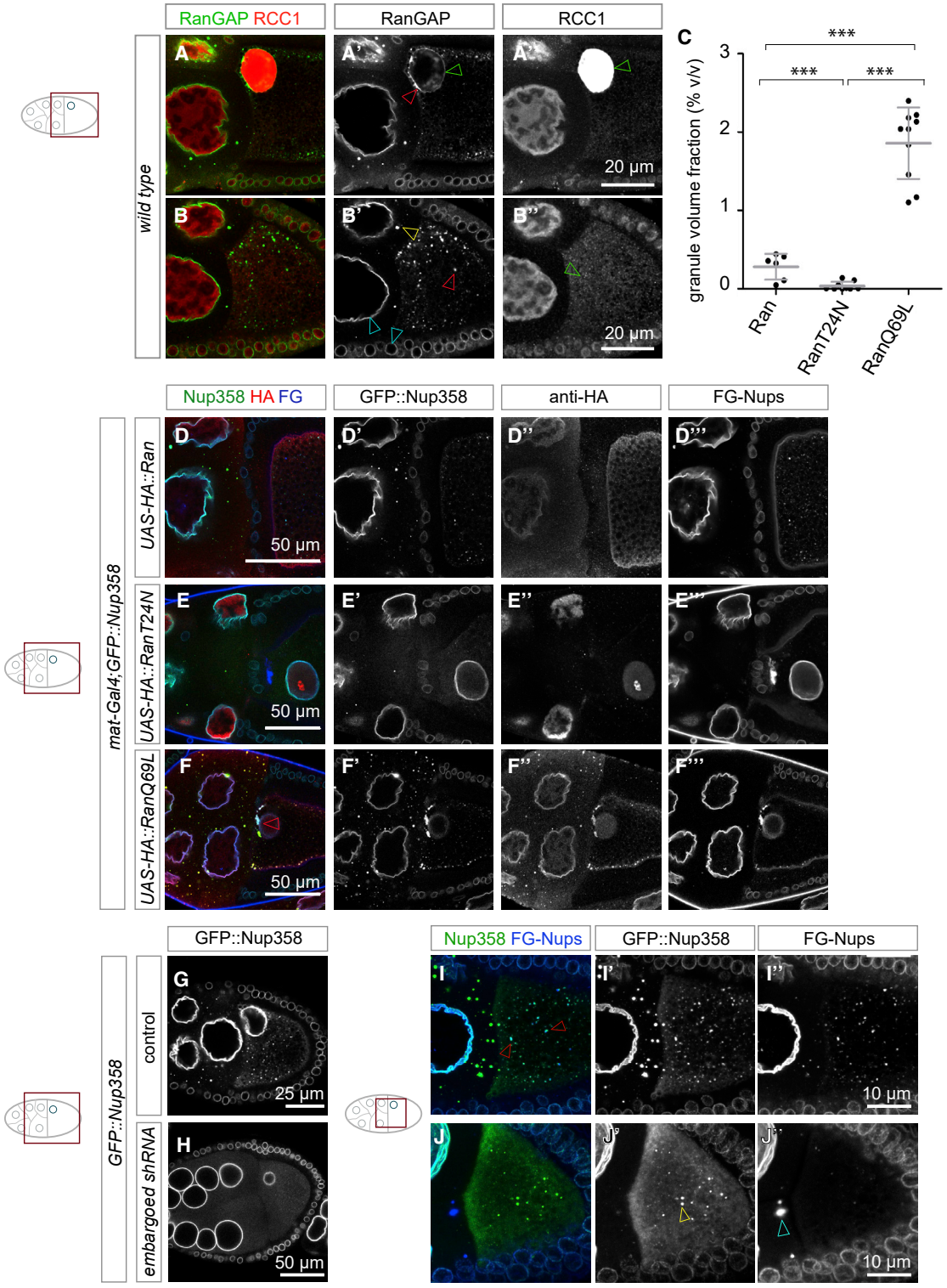

Figure 6. Ran and Crm1 Spatially Control Nup Condensation and AL Assembly

(A and B) RanGAP and RCC1 distributions in the egg chamber. Top views of fixed wild-type egg chambers stained with antibodies detecting RanGAP (A, A', B, and B') and the RanGEF RCC1 (A, A'', B, and B''). Shown in (A)–(A''), the oocyte nucleus is strongly enriched for nucleoplasmic RCC1 (green arrowhead in A'') but depleted for RanGAP at the NE (green arrowhead in A'), in comparison to nurse cell nuclei. Note that the strong RanGAP spot at the oocyte nucleus' anterior side is likely an AL at the NE (red arrowhead in A'). Shown in (B) and (B'), RanGAP localizes to the NE throughout the egg chamber (cyan arrowheads in B') to Nup358

(legend continued on next page)

MT dependent granule dynamics (Figure 7B'). Upon interaction, granules transfer material and assemble Nups onto available ER membrane, ultimately leading to the formation of larger stacks with multiple membrane sheets (Figure 7B' and 7C'). Those are inherited to the embryo where they supplement dividing nuclei with NPCs throughout early embryogenesis (Figure 7D).

Maternal AL Biogenesis Proceeds from Nup Condensates

The phase-separating properties of FG-Nups have been subject to extensive research *in vitro* (Hülsmann et al., 2012; Konishi and Yoshimura, 2019; Lemke, 2016). Here, we provide evidence for condensation of Nups *in vivo*. Several properties, namely the coalescence of Nup358 granules (Figures 2B, 2C, 4C, 4D and S2C), the transfer of material between granules (Figure 3B-3C' and Video S3), the high molecular mobility within granules (Figure S2C), and the contact shapes observed upon granule interactions (Figure 4A-4A'') are hallmarks of biomolecular condensates. Such condensates are defined as ''non-membranous organelles'' (Brangwynne, 2013). Although AL inherently contain stacked membrane sheets, they retain at least some characteristics of a phase separated condensate such as a milieu that is distinct from the surrounding cytoplasm. These findings underline the importance of phase separation at membranes that was also observed in other biological systems (Banjade and Rosen, 2014; Zeng et al., 2018).

Several lines of evidence, namely 1,6-hexanediol treatment, depletion of *BicD* and *embargoed,* and the interference with the Ran nucleotide status suggest that condensation of Nups into NPC precursor granules is critical for AL biogenesis. It is further underlined by the fact that Colchicine treatment counteracts the RanQ69L phenotype by reducing the number of MT-promoted granule interactions. Condensation concentrates NPC constituents in a constrained volume within the large ooplasm and might prevent unspecific interactions of soluble Nups. MT dynamics enhances interactions of otherwise unmixed, compositionally heterogeneous NPC precursor condensates and is a prerequisite for NPC assembly from condensed granules. It also prevents unwanted fusion and relaxation of compositionally homogeneous condensates of the same type (Bergeron-Sandoval et al., 2016). Facilitated interactions of granules could be of particular importance in the highly viscous ooplasm, where cytoskeleton-induced streaming is critical for the efficient distribution of various components (Quinlan, 2016).

Maternal AL Biogenesis Is Distinct from Both Canonical NPC Assembly Pathways

The two canonical NPC assembly pathways rely on the stepwise and orchestrated assembly of soluble Nups or subcomplexes onto either anaphase chromatin or the NE surface during interphase, respectively. However, these spatial cues are absent in the ooplasm and alternative mechanisms to locally concentrate assembly modules must be important. We believe that the condensation of Nups replaces the canonical cues, in line with previous work that had shown functions of natively unfolded FG-Nups to stabilize each other but also NPC scaffold components during yeast NPC assembly (Onischenko et al., 2017). Controlled interactions and material transfer between condensates might account for specific steps of assembly and even provide a certain order, although this concept remains to be further tested.

Our data strongly suggest Nup358 granules as assembly platforms, where NPCs are seeded onto ER membranes. Nup358 has no reported role in initiating the assembly process in both previously described pathways (Weberruss and Antonin, 2016). On the contrary, during interphase Nup358 assembles rather late onto the NPC scaffold (Otsuka et al., 2016). Although such information is not available for post-mitotic assembly, its mitotic localization to kinetochores could indicate an early role for Nup358 (Joseph et al., 2004). Indeed, Nup358 is of structural importance for the pore scaffold, given that its loss destabilizes the outer Y complex at the cytoplasmic ring at NE-NPCs (von Appen et al., 2015). It is thus conceivable that Nup358 could not only stabilize but also recruit scaffold components onto membranes. Post-mitotic and interphase NPC assembly are initiated by two distinct Nups, Elys and Nup153, respectively. Elys localizes the Y complex onto anaphase chromatin and is dispensable for interphase assembly but also for AL formation, given that its depletion induces AL (Franz et al., 2007). In contrast, Nup153 seeds NPCs during interphase assembly onto the inner nuclear membrane (Vollmer et al., 2015), and it has been suggested to have a similar role at the ER during AL biogenesis (Weberruss and Antonin, 2016). We, however, found that Nup153 is absent from AL in oocytes (Figure 2A).

Despite all molecular and conceptual differences, the common driving force for NPC biogenesis at and beyond the nucleus is Ran that coordinates the availability of Nups for assembly by dissociating them from NTRs (Walther et al., 2003). Nup358

granules in nurse cells (yellow arrowhead in B') and to AL (red arrowhead in B'). RCC1 is enriched in all nuclei and in the ooplasm (green arrowhead in B''), compared with nurse cell cytoplasm.

(C–F) Ran controls AL biogenesis and Nup condensation. Shown in (C) is the quantification of the cytosolic volume fraction [% (v/v)] of GFP::Nup358 condensates in egg chambers expressing GFP::Nup358 and Ran (n = 6 egg chambers), RanT24N (n = 9) or RanQ69L (n = 10). Bars represent mean ± STDV. Shown in (D)–(F''') are images from fixed egg chambers isolated from flies expressing GFP::Nup358 and HA::Ran (D–D'''), HA::RanT24N (E–E'''), or HA::RanQ69L (F–F'''), respectively and stained for FG-Nups detected by WGA-Alexa647. Compared with HA::Ran (D–D''), HA::RanT24N expression reduces GFP::Nup358 condensates (E and E') and AL (E and E'') whereas HA::RanQ69L, which co-localizes with GFP::Nup358 (F–F'') augments Nup358 condensates (F and F') and induces AL clusters at the anterior ooplasm (red arrowhead in F).

(G–J) The *crm1* homolog *embargoed* regulates Nup condensation. Stills from time lapse videos imaging egg chambers from GFP::Nup358 expressing control (G and I–I'') or *embargoed* shRNA-treated ovaries (H and J–J'') and injected with WGA-Alexa647 to label FG-Nups (I–J''). Shown in (G) and (H) is the depletion of *embargoed* abolishes condensation of GFP::Nup358 and AL formation (H) compared with controls (G). In (I) and (J), reversed Nup condensation in *embargoed* shRNA-induced egg chambers GFP::Nup358 condensed in oocytes (J and yellow arrowhead in J') into granules that were WGA negative (J''), whereas FG-Nups condensed in nurse cells (J and cyan arrowhead in J''). GFP- and WGA-positive AL (red arrowheads in I) as in oocytes of control ovaries were missing in egg chambers depleted for embargoed (J–J'').

See also Figure S6.

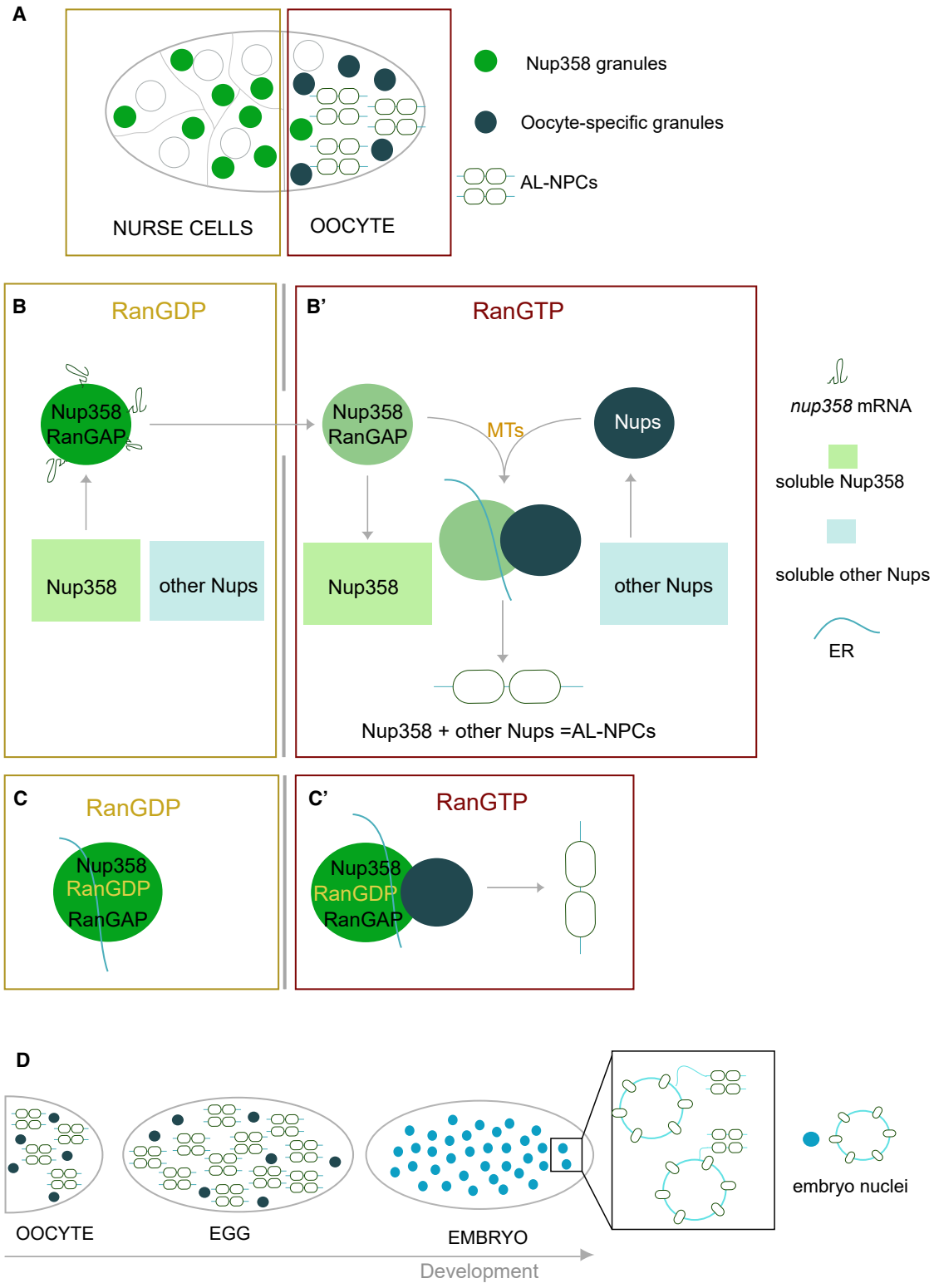

Figure 7. A Model for NPC Biogenesis beyond the Nuclear Compartment

(A) In a mid-oogenesis egg chamber Nup358 granules are prevalent in nurse cells, whereas oocyte-specific granules and AL occur in oocytes.

(B) A model for AL-NPC formation. Shown in (B), Nup358 condenses in nurse cells into Nup358 granules, possibly fed by local translation of its own mRNA. The absence of oocyte-specific granules and high amounts of RanGDP globally repress AL formation. Shown in (B'), in the ooplasm RanGTP stimulates

(legend continued on next page)

binds RanGAP and directly links the NPC to Ran activity. At the NE this is eminent to ensure a sharp Ran gradient and thus efficient nucleocytoplasmic transport. We show that this interaction is preserved beyond nuclei, because RanGAP strongly enriches at Nup358 granules in a Nup358-dependent manner (Figures S6A–B''). One might speculate that within the RanGTP milieu of the ooplasm, RanGAP induces a local Ran gradient at Nup358 granules that drives NPC biogenesis; conceptually similar to the nuclear compartment for interphase or postmitotic NPC assembly (Figure 7C and 7C'). Thereby, the observed progressive dilution of Nup358 and RanGAP at Nup358 granules in the oocyte could be important to drive their progression into AL (Figures S6C–S6E' and 7B). It might be caused by ooplasmic RanGTP that favors complex formation between Crm1 and Nup358. Although this would be consistent with the observed *embargoed* gene silencing phenotype (Figure 6G–6J''), the enhanced condensation of Nup358 upon global induction of RanGTP argues for an alternative interpretation: Nup358 functionally interacts with both, Importins and Crm1 under specific conditions (Gilistro et al., 2017; Ritterhoff et al., 2016). It is thus not clear how exactly it is being chaperoned. The phenotype observed under *embargoed* gene silencing conditions might be indirectly caused by disturbance of the spatial distribution of Ran and NTRs across nurse cells and oocytes, as indicated by the variety in phenotype across individuals. Yet it stresses the importance of spatially controlled Nup condensation to assemble AL-NPCs. In any scenario, NTR-mediated de-condensation of Nup358 and the consequent reduction of local RanGAP activity would regulate the progression of NPC biogenesis by determining the availability of soluble, ''assembly prone'' Nups and the degree of mixing at granule interfaces.

Various aspects of AL-NPC biogenesis are markedly different from both canonical NPC assembly pathways. During oogenesis, Nup condensation, local translation and MT dependent dynamics interplay with Ran activity in order to faithfully assemble AL in oocytes. They are inherited to the embryo where this pool of ready-made NPCs supplements nuclei during the rapid interphases of the blastoderm stage. Because AL are present in a plethora of species, similar mechanisms are likely to operate throughout animals.

STAR★METHODS

Detailed methods are provided in the online version of this paper and include the following:

SUPPLEMENTAL INFORMATION

Supplemental Information can be found online at https://doi.org/10.1016/j.cell.2019.09.022.

ACKNOWLEDGMENTS

We thank Drs. J. Baumbach, E. Lemke, J. Mahamid, and F. Melchior for critically reading this manuscript. We are grateful to Dr. J.M. Philippe in the laboratory of Dr. T. Lecuit who made the sqh-GFP::Kuk construct. We thank Drs. A. Akhtar, M. Frasch, K.S. McKim, M. Leptin, C. Samakovlis, and S. de Renzis for antibodies and fly lines, Dr. A. Reversi for fly transgenesis, and Drs F. Schnorrer and S. de Renzis for experimental advice. Stocks from the Bloomington *Drosophila* Stock center (NIH P40OD018537) were used in this study. The monoclonal antibody recognizing *Drosophila* gp210 was obtained from the Developmental Studies Hybridoma Bank created by the NICHD or the NIH and maintained at the University of Iowa. We acknowledge support from the European Molecular Biology Laboratory (EMBL)'s electron microscopy and advanced light microscopy core facilities. M.B. acknowledges funding by EMBL, the Max Planck Society and the European Research Council (724349-ComplexAssembly).

AUTHOR CONTRIBUTIONS

B.H. conceived the project, designed and performed experiments, analyzed data, wrote the manuscript, and supervised the project; A.S. conceived the project, designed and performed experiments, analyzed data, and wrote the manuscript; P.R. and H.B.-T. performed experiments and analyzed data; C.T. and I.G. analyzed data; A.E. and Y.S. supervised the project; M.B. conceived the project, designed experiments, wrote the manuscript, and supervised the project.

de-condensation and dilution of Nup358 and associated RanGAP from granules. Other Nups condense into oocyte-specific granules that interact with Nup358 granules in a MT-dependent manner allowing AL formation. AL-NPCs can only form from Nup condensates but not from soluble Nups.
(C) Due to its close association with RanGAP, condensed Nup358 induces a local RanGDP/GTP gradient in the RanGTP-enriched ooplasm (C') but not in the RanGDP milieu of the nurse cell cytoplasm (C). In analogy to the Ran gradient at the nuclear compartment, this might drive the de-condensation of Nups at the granule interface in the ooplasm, allowing AL-NPC assembly to proceed (C').
(D) AL-NPCs accumulate during oogenesis and are inherited to the embryo where they supplement the rapidly dividing nuclei during early embryogenesis with pre-assembled nuclear pores.

DECLARATION OF INTERESTS

The authors declare no competing interests.

Received: November 20, 2018
Revised: August 9, 2019
Accepted: September 20, 2019
Published: October 17, 2019

REFERENCES

Arganda-Carreras, I., Kaynig, V., Rueden, C., Eliceiri, K.W., Schindelin, J., Cardona, A., and Sebastian Seung, H. (2017). Trainable Weka Segmentation: a machine learning tool for microscopy pixel classification. Bioinformatics *33*, 2424–2426.

Banjade, S., and Rosen, M.K. (2014). Phase transitions of multivalent proteins can promote clustering of membrane receptors. eLife. https://doi.org/10.7554/eLife.04123.

Beck, M., and Hurt, E. (2017). The nuclear pore complex: understanding its function through structural insight. Nat. Rev. Mol. Cell Biol. *18*, 73–89.

Benaglia, T., Chauveau, D., Hunter, D.R., and Young, D.S. (2009). Mixtools: An R package for analyzing finite mixture models. J. Stat. Softw. *32*, 1–29.

Bergeron-Sandoval, L.-P., Safaee, N., and Michnick, S.W. (2016). Mechanisms and consequences of macromolecular phase separation. Cell *165*, 1067–1079.

Brandt, A., Papagiannouli, F., Wagner, N., Wilsch-Bräuninger, M., Braun, M., Furlong, E.E., Loserth, S., Wenzl, C., Pilot, F., Vogt, N., et al. (2006). Developmental control of nuclear size and shape by Kugelkern and Kurzkern. Curr. Biol. *16*, 543–552.

Brangwynne, C.P. (2013). Phase transitions and size scaling of membrane-less organelles. J. Cell Biol. *203*, 875–881.

Campbell, E.M., and Hope, T.J. (2015). HIV-1 capsid: the multifaceted key player in HIV-1 infection. Nat. Rev. Microbiol. *13*, 471–483.

Cesario, J., and McKim, K.S. (2011). RanGTP is required for meiotic spindle organization and the initiation of embryonic development in *Drosophila*. J. Cell Sci. *124*, 3797–3810.

Clark, I., Giniger, E., Ruohola-Baker, H., Jan, L.Y., and Jan, Y.N. (1994). Transient posterior localization of a kinesin fusion protein reflects anteroposterior polarity of the *Drosophila* oocyte. Curr. Biol. *4*, 289–300.

D'Angelo, M.A., Anderson, D.J., Richard, E., and Hetzer, M.W. (2006). Nuclear pores form de novo from both sides of the nuclear envelope. Science *312*, 440–443.

Dawlaty, M.M., Malureanu, L., Jeganathan, K.B., Kao, E., Sustmann, C., Tahk, S., Shuai, K., Grosschedl, R., and van Deursen, J.M. (2008). Resolution of sister centromeres requires RanBP2-mediated SUMOylation of topoisomerase IIalpha. Cell *133*, 103–115.

de Chaumont, F., Dallongeville, S., Chenouard, N., Hervé, N., Pop, S., Provoost, T., Meas-Yedid, V., Pankajakshan, P., Lecomte, T., Le Montagner, Y., et al. (2012). Icy: an open bioimage informatics platform for extended reproducible research. Nat. Methods *9*, 690–696.

Dickmanns, A., Kehlenbach, R.H., and Fahrenkrog, B. (2015). Nuclear pore complexes and nucleocytoplasmic transport: from structure to function to disease. Int. Rev. Cell Mol. Biol. *320*, 171–233.

Doucet, C.M., Talamas, J.A., and Hetzer, M.W. (2010). Cell cycle-dependent differences in nuclear pore complex assembly in metazoa. Cell *141*, 1030–1041.

Dultz, E., and Ellenberg, J. (2010). Live imaging of single nuclear pores reveals unique assembly kinetics and mechanism in interphase. J. Cell Biol. *191*, 15–22.

Dultz, E., Zanin, E., Wurzenberger, C., Braun, M., Rabut, G., Sironi, L., and Ellenberg, J. (2008). Systematic kinetic analysis of mitotic dis- and reassembly of the nuclear pore in living cells. J. Cell Biol. *180*, 857–865.

Forler, D., Rabut, G., Ciccarelli, F.D., Herold, A., Köcher, T., Niggeweg, R., Bork, P., Ellenberg, J., and Izaurralde, E. (2004). RanBP2/Nup358 provides a major binding site for NXF1-p15 dimers at the nuclear pore complex and functions in nuclear mRNA export. Mol. Cell. Biol. *24*, 1155–1167.

Franz, C., Walczak, R., Yavuz, S., Santarella, R., Gentzel, M., Askjaer, P., Galy, V., Hetzer, M., Mattaj, I.W., and Antonin, W. (2007). MEL-28/ELYS is required for the recruitment of nucleoporins to chromatin and postmitotic nuclear pore complex assembly. EMBO Rep. *8*, 165–172.

Frasch, M. (1991). The maternally expressed *Drosophila* gene encoding the chromatin-binding protein BJ1 is a homolog of the vertebrate gene Regulator of Chromatin Condensation, RCC1. EMBO J. *10*, 1225–1236.

Frey, S., Richter, R.P., and Görlich, D. (2006). FG-rich repeats of nuclear pore proteins form a three-dimensional meshwork with hydrogel-like properties. Science *314*, 815–817.

Gáspár, I., Sysoev, V., Komissarov, A., Ephrussi, A., Brendza, R., Serbus, L., Duffy, J., Saxton, W., Bullock, S., Ringel, I., et al. (2016). An RNA-binding atypical tropomyosin recruits kinesin-1 dynamically to oskar mRNPs. EMBO J. *289*, 2120–2122.

Gaspar, I., Wippich, F., and Ephrussi, A. (2017). Enzymatic production of single-molecule FISH and RNA capture probes. RNA *23*, 1582–1591.

Gáspár, I., Wippich, F., and Ephrussi, A. (2018). Terminal deoxynucleotidyl transferase mediated production of labeled probes for single-molecule FISH or RNA capture. Bio Protoc., 8.

Ghosh, S., Marchand, V., Gáspár, I., and Ephrussi, A. (2012). Control of RNP motility and localization by a splicing-dependent structure in oskar mRNA. Nat. Struct. Mol. Biol. *19*, 441–449.

Gilistro, E., de Turris, V., Damizia, M., Verrico, A., Moroni, S., De Santis, R., Rosa, A., and Lavia, P. (2017). Importin-β and CRM1 control a RANBP2 spatiotemporal switch essential for mitotic kinetochore function. J. Cell Sci. *130*, 2564–2578.

Görlich, D., and Kutay, U. (1999). Transport between the cell nucleus and the cytoplasm. Annu. Rev. Cell Dev. Biol. *15*, 607–660.

Gratz, S.J., Cummings, A.M., Nguyen, J.N., Hamm, D.C., Donohue, L.K., Harrison, M.M., Wildonger, J., and O'Connor-Giles, K.M. (2013). Genome engineering of *Drosophila* with the CRISPR RNA-guided Cas9 nuclease. Genetics *194*, 1029–1035.

Hampoelz, B., Mackmull, M.-T., Machado, P., Ronchi, P., Bui, K.H., Schieber, N., Santarella-Mellwig, R., Necakov, A., Andrés-Pons, A., Philippe, J.M., et al. (2016). Pre-assembled nuclear pores insert into the nuclear envelope during early development. Cell *166*, 664–678.

Hoelz, A., Debler, E.W., and Blobel, G. (2011). The structure of the nuclear pore complex. Annu. Rev. Biochem. *80*, 613–643.

Hülsmann, B.B., Labokha, A.A., and Görlich, D. (2012). The permeability of reconstituted nuclear pores provides direct evidence for the selective phase model. Cell *150*, 738–751.

Izquierdo, E., Quinkler, T., and De Renzis, S. (2018). Guided morphogenesis through optogenetic activation of Rho signalling during early *Drosophila* embryogenesis. Nat. Commun. *9*, 2366.

Joseph, J., Liu, S.-T., Jablonski, S.A., Yen, T.J., and Dasso, M. (2004). The RanGAP1-RanBP2 complex is essential for microtubule-kinetochore interactions in vivo. Curr. Biol. *14*, 611–617.

Katsani, K.R., Karess, R.E., Dostatni, N., and Doye, V. (2008). In vivo dynamics of *Drosophila* nuclear envelope components. Mol. Biol. Cell *19*, 3652–3666.

Kessel, R.G. (1983). The structure and function of annulate lamellae: porous cytoplasmic and intranuclear membranes. Int. Rev. Cytol. *82*, 181–303.

Klebe, C., Bischoff, F.R., Ponstingl, H., and Wittinghofer, A. (1995). Interaction of the nuclear GTP-binding protein Ran with its regulatory proteins RCC1 and RanGAP1. Biochemistry *34*, 639–647.

Knockenhauer, K.E., and Schwartz, T.U. (2016). The nuclear pore complex as a flexible and dynamic gate. Cell *164*, 1162–1171.

Konishi, H.A., and Yoshimura, S.H. (2019). Non-FG-Nups, ELYS and Nup35, coordinate an ordered assembly of FG-Nups on the scaffold of the nuclear pore complex. bioRxiv, 506469.

Kremer, J.R., Mastronarde, D.N., and McIntosh, J.R. (1996). Computer visualization of three-dimensional image data using IMOD. J. Struct. Biol. *116*, 71–76.

Kukulski, W., Schorb, M., Welsch, S., Picco, A., Kaksonen, M., and Briggs, J.A.G. (2011). Correlated fluorescence and 3D electron microscopy with high sensitivity and spatial precision. J. Cell Biol. *192*, 111–119.

Kusano, A., Staber, C., and Ganetzky, B. (2002). Segregation distortion induced by wild-type RanGAP in *Drosophila*. Proc. Natl. Acad. Sci. USA *99*, 6866–6870.

Legland, D., Arganda-Carreras, I., and Andrey, P. (2016). MorphoLibJ: integrated library and plugins for mathematical morphology with ImageJ. Bioinformatics *32*, 3532–3534.

Lemke, E.A. (2016). The multiple faces of disordered nucleoporins. J. Mol. Biol. *428* (10 Pt A), 2011–2024.

Mach, J.M., and Lehmann, R. (1997). An Egalitarian-BicaudalD complex is essential for oocyte specification and axis determination in Drosophila. Genes Dev. *11*, 423–435.

Matunis, M.J., Wu, J., and Blobel, G. (1998). SUMO-1 modification and its role in targeting the Ran GTPase-activating protein, RanGAP1, to the nuclear pore complex. J. Cell Biol. *140*, 499–509.

Mendjan, S., Taipale, M., Kind, J., Holz, H., Gebhardt, P., Schelder, M., Vermeulen, M., Buscaino, A., Duncan, K., Mueller, J., et al. (2006). Nuclear pore components are involved in the transcriptional regulation of dosage compensation in *Drosophila*. Mol. Cell *21*, 811–823.

Milles, S., Huy Bui, K., Koehler, C., Eltsov, M., Beck, M., and Lemke, E.A. (2013). Facilitated aggregation of FG nucleoporins under molecular crowding conditions. EMBO Rep. *14*, 178–183.

Norrander, J., Kempe, T., and Messing, J. (1983). Construction of improved M13 vectors using oligodeoxynucleotide-directed mutagenesis. Gene *26*, 101–106.

Okada, E., and Waddington, C.H. (1959). The submicroscopic structure of the *Drosophila* egg. J. Embryol. Exp. Morphol. *7*, 583–597.

Onischenko, E., Tang, J.H., Andersen, K.R., Knockenhauer, K.E., Vallotton, P., Derrer, C.P., Kralt, A., Mugler, C.F., Chan, L.Y., Schwartz, T.U., et al. (2017). Natively unfolded FG repeats stabilize the structure of the nuclear pore complex. Cell. https://doi.org/10.1016/j.cell.2017.09.033.

Otsuka, S., Bui, K.H., Schorb, M., Hossain, M.J., Politi, A.Z., Koch, B., Eltsov, M., Beck, M., and Ellenberg, J. (2016). Nuclear pore assembly proceeds by an inside-out extrusion of the nuclear envelope. eLife *5*, 76.

Paul-Gilloteaux, P., Heiligenstein, X., Belle, M., Domart, M.-C., Larijani, B., Collinson, L., Raposo, G., and Salamero, J. (2017). eC-CLEM: flexible multidimensional registration software for correlative microscopies. Nat. Methods *14*, 102–103.

Quinlan, M.E. (2016). Cytoplasmic Streaming in the *Drosophila* Oocyte. Annu. Rev. Cell Dev. Biol. *32*, 173–195.

Raices, M., and D'Angelo, M.A. (2012). Nuclear pore complex composition: a new regulator of tissue-specific and developmental functions. Nat. Rev. Mol. Cell Biol. *13*, 687–699.

Raj, A., van den Bogaard, P., Rifkin, S.A., van Oudenaarden, A., and Tyagi, S. (2008). Imaging individual mRNA molecules using multiple singly labeled probes. Nat. Methods *5*, 877–879.

Rasala, B.A., Ramos, C., Harel, A., and Forbes, D.J. (2008). Capture of AT-rich chromatin by ELYS recruits POM121 and NDC1 to initiate nuclear pore assembly. Mol. Biol. Cell *19*, 3982–3996.

Ribbeck, K., and Görlich, D. (2002). The permeability barrier of nuclear pore complexes appears to operate via hydrophobic exclusion. EMBO J. *21*, 2664–2671.

Ritterhoff, T., Das, H., Hofhaus, G., Schröder, R.R., Flotho, A., and Melchior, F. (2016). The RanBP2/RanGAP1*SUMO1/Ubc9 SUMO E3 ligase is a disassembly machine for Crm1-dependent nuclear export complexes. Nat. Commun. *7*, 11482.

Röper, K. (2007). Rtnl1 is enriched in a specialized germline ER that associates with ribonucleoprotein granule components. J. Cell Sci. *120*, 1081–1092.

Roth, P., Xylourgidis, N., Sabri, N., Uv, A., Fornerod, M., and Samakovlis, C. (2003). The *Drosophila* nucleoporin DNup88 localizes DNup214 and CRM1 on the nuclear envelope and attenuates NES-mediated nuclear export. J. Cell Biol. *163*, 701–706.

RStudio Team (2015). RStudio: Integrated Development for R, Boston, MA.

Ryan, K.J., McCaffery, J.M., and Wente, S.R. (2003). The Ran GTPase cycle is required for yeast nuclear pore complex assembly. J. Cell Biol. *160*, 1041–1053.

Schindelin, J., Arganda-Carreras, I., Frise, E., Kaynig, V., Longair, M., Pietzsch, T., Preibisch, S., Rueden, C., Saalfeld, S., Schmid, B., et al. (2012). Fiji: an open-source platform for biological-image analysis. Nat. Methods *9*, 676–682.

Sommer, C., Straehle, C., Kothe, U., and Hamprecht, F.A. (2011). Ilastik: Interactive learning and segmentation toolkit. In Proceedings - International Symposium on Biomedical Imaging.

Splinter, D., Tanenbaum, M.E., Lindqvist, A., Jaarsma, D., Flotho, A., Yu, K.L., Grigoriev, I., Engelsma, D., Haasdijk, E.D., Keijzer, N., et al. (2010). Bicaudal D2, dynein, and kinesin-1 associate with nuclear pore complexes and regulate centrosome and nuclear positioning during mitotic entry. PLoS Biol. *8*, e1000350.

St Johnston, D. (2005). Moving messages: the intracellular localization of mRNAs. Nat. Rev. Mol. Cell Biol. *6*, 363–375.

Suter, B., Romberg, L.M., and Steward, R. (1989). Bicaudal-D, a *Drosophila* gene involved in developmental asymmetry: localized transcript accumulation in ovaries and sequence similarity to myosin heavy chain tail domains. Genes Dev. *3* (12A), 1957–1968.

Swan, A., and Suter, B. (1996). Role of Bicaudal-D in patterning the *Drosophila* egg chamber in mid-oogenesis. Development *122*, 3577–3586.

Thévenaz, P., Ruttimann, U.E., and Unser, M. (1998). A pyramid approach to subpixel registration based on intensity. IEEE Trans. Image Process. *7*, 27–41.

Ungricht, R., and Kutay, U. (2017). Mechanisms and functions of nuclear envelope remodelling. Nat. Rev. Mol. Cell Biol. *18*, 229–245.

Vollmer, B., Lorenz, M., Moreno-Andrés, D., Bodenhöfer, M., De Magistris, P., Astrinidis, S.A., Schooley, A., Flötenmeyer, M., Leptihn, S., and Antonin, W. (2015). Nup153 recruits the Nup107-160 complex to the inner nuclear membrane for interphasic nuclear pore complex assembly. Dev. Cell *33*, 717–728.

von Appen, A., Kosinski, J., Sparks, L., Ori, A., DiGuilio, A.L., Vollmer, B., Mackmull, M.-T., Banterle, N., Parca, L., Kastritis, P., et al. (2015). *In situ* structural analysis of the human nuclear pore complex. Nature *526*, 140–143.

Walther, T.C., Askjaer, P., Gentzel, M., Habermann, A., Griffiths, G., Wilm, M., Mattaj, I.W., and Hetzer, M. (2003). RanGTP mediates nuclear pore complex assembly. Nature *424*, 689–694.

Waterman-Storer, C.M., and Salmon, E.D. (1998). Endoplasmic reticulum membrane tubules are distributed by microtubules in living cells using three distinct mechanisms. Curr. Biol. *8*, 798–806.

Weberruss, M., and Antonin, W. (2016). Perforating the nuclear boundary – how nuclear pore complexes assemble. J. Cell Sci. https://doi.org/10.1242/jcs.194753.

Wickham, H. (2009). Introduction. In Ggplot2 (New York, NY: Springer New York), pp. 1–7.

Zeng, M., Chen, X., Guan, D., Xu, J., Wu, H., Tong, P., and Zhang, M. (2018). Reconstituted Postsynaptic Density as a Molecular Platform for Understanding Synapse Formation and Plasticity. Cell *174*, 1172–1187.e16.

STAR★METHODS

KEY RESOURCES TABLE

REAGENT or RESOURCE	SOURCE	IDENTIFIER
Antibodies		
Mouse monoclonal anti-BJ1 (RCC1) (1:20 dilution)	Frasch, 1991	BJ43
Rabbit polyclonal anti-RanGAP (1:500 dilution)	Sigma-Aldrich	Cat#ABN1674
Rabbit anti-Nup153 (1:500 dilution)	Mendjan et al., 2006	N/A
Rabbit anti-Nup214 (1:500 dilution)	Roth et al., 2003	N/A
Mouse monoclonal anti-Gp210 (1:50 dilution)	Developmental Studies Hybridoma Bank	DSHB Cat#agp26.10; RRID: AB_528270
Mouse monoclonal anti-Nuclear Pore Complex Proteins mAb414 (1:500 dilution)	BioLegend	Covance Cat#MMS-120R-200; RRID: AB_10718044
Rabbit polyclonal anti-HA (1:500 dilution)	Sigma-Aldrich	Sigma-Aldrich Cat#H6908; RRID: AB_260070
Wheat Germ Agglutinin, Alexa Fluor™ 647 Conjugate (1:500 dilution)	ThermoFisher Scientific	Cat#W32466
Wheat Germ Agglutinin, Tetramethylrhodamine Conjugate (1:500 dilution)	ThermoFisher Scientific	Cat#W849
Chemicals, Peptides, and Recombinant Proteins		
1,6-Hexanediol (99%)	Sigma-Aldrich	Cat#240117
Puromycin dihydrochloride	ThermoFisher	Cat#A1113803
Cycloheximide	Sigma-Aldrich	Cat#C1988
Homoharringtonine	Sigma-Aldrich	Cat#SML1091
Colchicine	Sigma-Aldrich	Cat#C9754
Experimental Models: Organisms/Strains		
D. melanogaster: w[1118]	Bloomington *Drosophila* Stock Center	BDSC Cat#3605; RRID: BDSC_3605
D. melanogaster: w*wg^{Sp-1}/CyO;P{mGFP-Nup107.K}9.1	Bloomington *Drosophila* Stock Center, Katsani et al., 2008	BDSC Cat#35514; RRID: BDSC_35514
D. melanogaster: w*wg^{Sp-1}/CyO;P{mRFP-Nup107.K}7.1	Bloomington *Drosophila* Stock Center, Katsani et al., 2008	BDSC Cat#35517; RRID: BDSC_35517
D. melanogaster: w*Nup107^{E8}/CyO;P{mRFP-Nup107.K}7.1, P{His2Av$^{T:Avic\setminus GFP\text{-}S65T}$}62A	Bloomington *Drosophila* Stock Center, Katsani et al., 2008	BDSC Cat#35518; RRID: BDSC_35518
D. melanogaster: P[w+, sqhp > Gap43::mCherry]/Fm7; Sb/TM6 Tb	Izquierdo et al., 2018	N/A
D. melanogaster: y[1] sc[*] v[1]; P{y[+t7.7] v[+t1.8] = TRIP.HMS00865}attP2	Bloomington *Drosophila* Stock Center	BDSC Cat#34967; RRID: BDSC_34967
D. melanogaster: y^{1} sc[*] v[1]; sev^{21}P{TRIP.HMS00991}attP2	Bloomington *Drosophila* Stock Center	BDSC Cat#34021; RRID: BDSC_34021
D. melanogaster: y^{1} sc[*] v[1]; sev^{21}P{TRIP.HMS02622}attP40	Bloomington *Drosophila* Stock Center	BDSC Cat#35405; RRID: BDSC_35405
D. melanogaster: y[1] sc[*] v[1]; P{y[+t7.7] v[+t1.8] = TRiP.GL00094}attP2	Bloomington *Drosophila* Stock Center	BDSC Cat#35573; RRID: BDSC_35573
D. melanogaster: P{w^{+},nanosGal4:VP16}; y^{1}w^{67c23}; P{w^{+},UASp-HA(3).Ran^{Q69L}}	Cesario and McKim, 2011	N/A
D. melanogaster: P{w^{+},UASp-HA(3).Ran^{T24N}}	Cesario and McKim, 2011	N/A
D. melanogaster: P{w^{+},UASp-HA(3).Ran}	Cesario and McKim, 2011	N/A

(*Continued on next page*)

Continued

REAGENT or RESOURCE	SOURCE	IDENTIFIER
D. melanogaster: w[*];P{w[+mC] = UASp-RFP.KDEL}10/TM3, Sb[1]	Bloomington *Drosophila* Stock Center	BDSC Cat#30909; RRID: BDSC_30909
D. melanogaster: w[1118]; PBac{y[+mDint2] = vas-Cas9}VK00027	Bloomington *Drosophila* Stock Center	BDSC Cat#51324; RRID: BDSC_51324
D. melanogaster: w[*]; P{w[+mC] = UAS-ChRFP::Tub}2	Bloomington *Drosophila* Stock Center	BDSC Cat#25774; RRID: BDSC_25774
D. melanogaster: w[1118]; P{w[+mC] = Gal4::VP16-nos.UTR] CG6325 [MVD1],P[w[+mC] = UASp-GFPS65C-alphaTub84B}3	Bloomington *Drosophila* Stock Center	BDSC Cat#7253; RRID: BDSC_7253
D. melanogaster: emGFP::nup358 PBac{y[+mDint2] = vas-Cas9}VK00027	This study	N/A
D. melanogaster: w[*]; P{w[+mC] = sqhP-EGFP::kuk}	This study	N/A
Oligonucleotides		
smFISH probes, see Table S1	This study	N/A
AS375 (sgRNA fwd primer): CTTCGTTTACAACGCGAAAAGAAG	This study	N/A
AS376 (sgRNA rev primer): AAACCTTCTTTTCGCGTTGTAAAC	This study	N/A
Recombinant DNA		
pU6-BbsI-chiRNA	Gratz et al., 2013	Addgene Cat#45946; RRID: Addgene_45946
pUC19	Norrander et al., 1983	Addgene Cat#50005; RRID: Addgene_50005
pAS095 (pUC19-nup358_homology-loxP-GMR-3P3-EGFP-tubulin3'UTR-loxP-emGFP-nup358_homology)	This study	N/A
pC4-SqhP-EGFP::Kuk	This study	N/A
Software and Algorithms		
FIJI	Schindelin et al., 2012	http://fiji.sc
Ilastik (v 1.3.2)	Sommer et al., 2011	https://ilastik.org
MultiStackReg (v 1.45) (FIJI plugin)	Thévenaz et al., 1998	http://bradbusse.net/sciencedownloads.html
IMOD	Kremer et al., 1996	https://bio3d.colorado.edu/imod/
Icy	de Chaumont et al., 2012	http://icy.bioimageanalysis.org/
ec-CLEM (Icy plugin)	Paul-Gilloteaux et al., 2017	http://icy.bioimageanalysis.org/plugin/ec-clem/
Trainable Weka Segmentation (FIJI plugin)	Arganda-Carreras et al., 2017	https://imagej.net/Trainable_Weka_Segmentation
Huygens Essential	Scientific Volume Imaging, Hilversum, the Netherlands	https://svi.nl/Huygens-Essential
Rstudio	RStudio Team, 2015	https://www.rstudio.com/
_xsPT (FIJI plugin)	Gaspar et al., 2017; Gáspár et al., 2018	https://github.com/Xaft/xs/blob/master/_xs.jar
ggplot2 (R package)	Wickham, 2009	https://ggplot2.tidyverse.org/
mixtools (R package)	Benaglia et al., 2009	https://cran.r-project.org/web/packages/mixtools/
MorphoLibJ (FIJI plugin)	Legland et al., 2016	https://imagej.net/MorphoLibJ

LEAD CONTACT AND MATERIALS AVAILABILITY

Further information and requests for resources and reagents should be directed to and will be fulfilled by the Lead Contact, Martin Beck (martin.beck@biophys.mpg.de).

All unique/stable reagents generated in this study are available from the Lead Contact with a completed Materials Transfer Agreement.

EXPERIMENTAL MODEL AND SUBJECT DETAILS

Drosophila melanogaster fly stocks were maintained at 23°C on standard cornmeal agar in round-bottom vials. 24 h before experiments, a required amount of young (< 7 d) female and roughly half as many male flies were transferred to a fresh vial supplemented with freshly prepared yeast paste.

METHOD DETAILS

Fly strains and antibodies

The following fly lines were used in this study: *w*wg^{Sp-1}/CyO;P{mGFP-Nup107.K}9.1* (Katsani et al., 2008) (BL-35514); *w*wg^{Sp-1}/CyO;P{mRFP-Nup107.K}7.1* (Katsani et al., 2008) (BL-35517); *w*Nup107^{E8}/CyO;P{mRFP-Nup107.K}7.1, P{His2Av$^{T:Avic\GFP-S65T}$}62A* (Katsani et al., 2008) (BL-35518); *P[w+, sqhp > Gap43::mCherry]/Fm7; Sb/TM6 Tb* (Izquierdo et al., 2018); y[1] *sc[*] v[1]; P{y[+t7.7] v[+t1.8] = TRIP.HMS00865}attP2* (BL-34967); *y^{1} sc[*] v[1]; sev^{21}P{TRIP.HMS00991}attP2* (BL-34021); *y^{1} sc[*] v[1]; sev^{21}P{TRIP.HMS02622}attP40* (BL-35405); *y[1] sc[*] v[1]; P{y[+t7.7] v[+t1.8] = TRiP.GL00094}attP2 (BL-35573)*; *P{w^{+},nanosGal4:VP16}*; *y^{1}w^{67c23} ; P{w^{+},UASp-HA(3).Ran^{Q69L}}* (Cesario and McKim, 2011); *P{w^{+},UASp-HA(3).Ran^{T24N}}* (Cesario and McKim, 2011); *P{w^{+},UASp-HA(3).Ran}* (Cesario and McKim, 2011); *w[*];P{w[+mC] = UASp-RFP.KDEL}10/TM3, Sb[1] (BL-30909);* w[1118]; *PBac{y[+mDint2] = vas-Cas9}VK00027* (BL-51324); *w[*]; P{w[+mC] = UAS-ChRFP-Tub}2 (BL-25774).* All ectopic expressions including induction of shRNA were induced by crossing males of the respective genotype to females of *w[1118]; P{w[+mC] = Gal4::VP16-nos.UTR] CG6325 [MVD1],P[w[+mC] = UASp-GFPS65C-alphaTub84B}3 (BL-7253).*

For immunostainings, fixed egg chambers were proceeded for incubation with the following primary antibodies: mouse anti-RCC1 (BJ-1)(1:20) (Frasch, 1991); rabbit anti-RanGAP (1:500, Millipore) (Kusano et al., 2002), rabbit anti-Nup153 (1:500) (Mendjan et al., 2006), rabbit anti-Nup214 (1:500) (Roth et al., 2003), mouse anti-Gp210 AGP26.10 (1:50) (DSHB), mouse anti-Nuclear Pore Complex Proteins mAb414 (1:500, BioLegends), rabbit anti-HA (1:500, Sigma, H6908). WGA-Alexa647 (2 μg/mL, Thermo Fisher). Secondary antibodies were AlexaFluor conjugates (1:500, Life Technologies) as described below.

Live imaging and injections

Ovaries of the desired genotype were dissected in BRB80 buffer (80mM PIPES pH = 6,9, 1mM EGTA, 2mM $MgCl_2$) and subsequently mounted onto coverslips in a drop of Schneider's medium supplemented with 10% fetal calf serum and insulin (200 μg/mL). A drop of Voltalef 10S oil (vWF) was placed next to the dissected ovaries and individual ovarioles were pulled under the oil with fine tungsten needles (Ghosh et al., 2012). If required, individual egg chambers were injected under oil with WGA-Alexa647 (100 μg/mL). Egg chambers were imaged at RT on an inverted LSM 780 confocal microscope (Zeiss) with a 63x/1,4 NA oil immersion objective. For *ex vivo* squash preparations individual egg chambers were isolated for live-imaging as described above and the posterior (oocyte) portion was squashed in the halocarbon oil phase with a tungsten needle onto the coverslip and subsequently imaged. Colchicine treatment to depolymerize microtubules was applied by feeding flies of the desired genotype with yeast paste containing 100 μg/mL colchicine in 1% Sucrose for 16 h after being starved for 8 h.

Embryos were dechorionated, aligned and glued onto a coverslip, dried on silica for 8 min and overlaid with Halocarbon oil before injection with WGA-Alexa647 in water (100 μg/mL). Embryos were imaged similar to egg chambers.

Fluorescent Recovery After Photobleaching

For live Fluorescence Recovery After Photobleaching (FRAP) recordings, GFP::Nup358 females were prepared as described above. For *ex vivo* recordings, nurse cells of stage 10 egg chambers that were pulled under Voltalef 10S oil (vWF) and carefully squashed with tungsten needles to form a pocket of cytoplasm under the oil. Time series were recorded on a Olympus FV3000 confocal microscope using a 60x/1.3 NA silicone objective, excited by a 488 nm excitation laser and with a frame rate of 140 ms for *ex vivo* and 260 ms for *in vivo* measurements. Photo bleaching was performed via the same laser at maximum output in a single diffraction limited confocal volume within the granule for one frame without interruption. Before bleaching, 10 frames were acquired and after bleaching time-lapse observation was continued for 200 frames. Time series of FRAP recordings were imported into FIJI and centered in X/Y using the MultiStackReg plugin (Thévenaz et al., 1998). Single frames of *in vivo* and *ex vivo* time series were displayed and a kymograph constructed by averaging 5 frames traversing the granule.

Immunofluorescence

For immunostainings described in Figure 2A-2A''and Figure 6A-B'', dissected wild type ovaries were fixed for 30 min with 4% formaldehyde in PBS, incubated for 1 h with PBS, 1%Triton X-100, blocked in blocking buffer (PBS, 0,2% Triton X-100) for 1 h and incubated with primary antibodies diluted in blocking buffer o/n at 4 degrees. Secondary antibodies were applied in blocking buffer for 2 h at RT and samples were mounted after 3 times 10 min washes onto coverslips using Vectashield.

For immunostainings represented in all other figures, ovaries of the respective genotype were collected, rinsed once in 1x BRB80 and fixed in 2% PFA, 0.05% Triton X-100 in PBS on an orbital shaker for 20 min. For Figures S2A-S2B'', ovaries were incubated in imaging buffer (10% FCS, 0.4 mg/mL insulin in Schneider's medium) supplemented with 5% 1,6-hexanediol or no additives as control for 15 min on an orbital shaker prior to fixation. Fixative was then removed, specimen were washed 3x for 5 min each in PBSTX

(0.1% Triton X-100 in PBS), transferred to a 37°C ThermoTop incubator and incubated in 2x SSC, 0.1% Triton X-100, 0.2 mg/mL BSA for 14 – 18 h. Ovaries were then incubated with primary antibodies in 2x SSCTX (2x SSC, 0.1% Triton X-100) for 3 - 4 h at room temperature on a roller drum. After a short rinse and three washes for 10 min each in 2x SSCTX while rotating, incubation of secondary antibodies was performed for 2 h. Ovaries were again rinsed once and washed 3x for 10 min in 2x SSCTX while rotating and finally mounted in 50 μL ProLong Diamond mounting medium (Life Technologies, P36961). Sample imaging was identical to smFISH as described below.

Correlative Light and Electron Microscopy

For Correlative Light and Electron Microscopy (CLEM) analysis, *Drosophila* egg chambers were dissected from ovaries in Schneider's medium and high-pressure frozen (HPM010, AbraFluid) in the same medium containing 20% Ficoll (70kDa) as a cryoprotectant. The samples were then freeze-substituted (EM-AFS2 - Leica Microsystems) with 0.1% Uranyl Acetate (UA) in acetone at −90°C for 48 h. The temperature was then raised to −45°C at 3.5°C/h and samples were further incubated for 5 h. After rinsing in acetone, the samples were infiltrated in Lowicryl HM20 resin, while raising the temperature to −25°C and left to polymerize under UV light for 48 h at −25°C and for further 9 h while the temperature was gradually raised to 20°C (5°C/h). Thick sections (300nm) were cut from the polymerized resin block and picked up on carbon coated mesh grids. The fluorescence microscopy (FM) imaging of the sections was carried out as previously described (Kukulski et al., 2011) using a widefield fluorescence microscope (Olympus IX81) equipped with an Olympus PlanApo 100X 1.40 NA oil immersion objective.

After post-staining, tilt series of the areas of interest were acquired using a FEI TECNAI F30 TEM and tomograms were reconstructed using the software package IMOD (Kremer et al., 1996). Correlation between light and electron micrographs was carried out with the plugin ec-CLEM (Paul-Gilloteaux et al., 2017) of the software platform Icy (de Chaumont et al., 2012). The coordinates of pairs of corresponding features in the 2 images modalities were used to calculate a linear transformation, which allowed to map the coordinates of the fluorescent spots of interest and to overlay them on the electron micrograph.

Focused Ion Beam-Scanning Electron Microscopy

For Focused Ion Beam-Scanning Electron Microscopy (FIB-SEM) analysis, dissected egg chambers were high-pressure frozen as described above and freeze substituted with 1% Osmium tetroxide 0.2% UA 5% water in acetone at −90°C for 64 h. The temperature was then raised to −30°C at 5°C/h and the samples were incubated at this temperature for 4 h, before raising the temperature to +20°C (5°C/h) and incubating for 5 more h. Sample were then rinsed in acetone and incubated in 0.1% TCH (Thiocarbonohydrazide) 10% water in acetone for 20min at room temperature. After rinsing, samples were further processed with 2% Osmium tetroxide in acetone in a PELCO Biowave Pro microwave processor (Ted Pella, Inc.) and then embedded in Durcupan ACM epoxy resin (Sigma Aldrich). The resin blocks were pre-trimmed with a Leica UC7 ultramicrotome in order to expose the region of interest and then a volume of ∼1200 μm^3 (12x11x12 μm) was acquired with a Zeiss Crossbeam 540 FIB-SEM microscope at 5 nm isotropic resolution. The image stack was aligned using custom java code for cross-correlation between manually selected regions in subsequent slices. Manual segmentation of AL was performed with IMOD. In addition, automated segmentation of AL and ribosomes was performed using a modified version of Fiji's trainable segmentation plugin (Arganda-Carreras et al., 2017).

smFISH probe synthesis

smFISH probes were produced as described in (Gaspar et al., 2017). Non-overlapping 18 - 22 nt long ssDNA oligonucleotides complementary to the target transcript were designed either via the Stellaris® online probe designer (https://www.biosearchtech.com/stellaris-designer) or manually aiming for 45 – 60% GC content, similar melting temperature, as well as presence of a 3' U to allow hybridization of incorporated ddUTP during probe synthesis. For preparation of dye-conjugated ddUTP, Amino-11-ddUTP (Lumiprobe, A5040) was combined with two-fold molar excess of dye-NHS-ester (Atto 565 NHS-ester, ATTO-TEC, AD 565-31; Atto 633 NHS-ester, ATTO-TEC, AD 633-31) and 100 mM $NaHCO_3$ (pH 8.3) and incubated for 3 h in the dark at room temperature. NHS-esters were generally dissolved in anhydrous DMSO to 20 – 40 mM and entirely conjugated to Amino-11-ddUTP. In order to quench any unreacted ester groups, Tris HCl (pH 7.4) was added to 10 mM final concentration and the reaction mixture was adjusted to 2 - 5 mM concentration with nuclease-free water. Oligonucleotides targeting the same transcript were pooled to a concentration of 250 μM/probe and 1 nmol was mixed with 12 or 6 mU/pmol ssDNA of Terminal deoxynucleotidyl transferase (TdT) (ThermoFisher, EP0162), 1x TdT Buffer and 5 or 3-fold molar excess of Atto 565 or Atto 633 conjugated ddUTP respectively. Enzymatic labeling was performed at 37°C for 16 – 18 h. Labeled probes were then purified by ethanol precipitation. For this, 2 μg/mL linear acrylamide and 300 mM sodium acetate (pH 5.5) as well as nuclease-free water was added to 200 μl, followed by addition of 800 μL pre-chilled −20°C ethanol. Precipitation was performed for 20 min at −80°C followed by 20 min centrifugation at 13,000 g and 4°C. The supernatant was removed and the pellet was vortexed in 1 mL −20°C 80% ethanol and pelleted again at 13,000 g, 4°C for 5 min. The pellet was transferred to a new centrifuge tube and detached and pelleted two more times in the same tube. The ethanol was then removed and the remaining liquid was aspirated by gentle heating for 5 min at 37°C. The dried pellet was finally resuspended in 25 μL nuclease-free water and the degree of labeling, concentration, as well as the loss was determined via absorption measurements on a NanoDrop 2000 according to formula (1), (2) and (3) in (Gaspar et al., 2017), respectively.

smFISH hybridization and imaging

All steps were performed at room temperature unless indicated otherwise.

Ovaries of the indicated genotype were dissected into 1x BRB80 buffer and wherever indicated were incubated in imaging buffer (10% FCS, 0.4 mg/mL insulin in Schneider's medium) supplemented with 100 μg/mL cycloheximide, 200 μM puromycin, 5 μM homoharringtonine, or no additives as control for 15 min on an orbital shaker. Colchicine treatment was performed by feeding flies colchicine-supplemented yeast paste as described above. For non-perturbation smFISH experiments, this step was omitted. After incubation, ovaries were rinsed once in 1x BRB80 and fixed in 2% PFA, 0.05% Triton X-100 in PBS on an orbital shaker for 20 min. Fixative was removed and samples were washed 3x for 5 min each in PBSTX (0.1% Triton X-100 in PBS), followed by a 20 min pre-hybridization in wash buffer (2x SSC, 10% formamide, 0.1% Tween-20) under constant rocking. In the meantime, hybridization buffer (2x SSC, 10% formamide, 0.1% Tween-20, 2 mM vanadyl ribonucleoside complex, 100 μg/mL salmon sperm DNA, 10% dextran sulfate, 20 μg/mL BSA) was prepared, smFISH probes coupled to either Atto 565 or Atto 633 were added to a final concentration of 1 nM per individual probe, and pre-heated to 37°C. A full list of probes used in this study is available in the attached spreadsheet (Table S1). Samples were transferred to a 37°C ThermoTop incubator, wash buffer was replaced with hybridization buffer plus smFISH probes and hybridized for 14–18 h. The hybridization solution was removed and rinsed with 500 μL pre-warmed (37°C) wash buffer, followed by two washes for 30 min at 37°C and 900 rpm. Whenever indicated, either TMR or Alexa 647-conjugated wheat germ agglutinin (WGA) (ThermoFisher, W849 or W32466) was added to a final concentration of 2 μg/mL to the second wash. Wash buffer was removed and ovaries were transferred to room temperature and briefly rinsed 4x with PBST (0.1% Tween-20 in PBS). Ovaries were mounted in 50 μL ProLong Diamond mounting medium (Life Technologies, P36961).

Image stacks were acquired on a Leica SP8 confocal microscope and a 63x/1.4 NA oil immersion objective and wherever indicated, were deconvolved using the Huygens Essential software package.

Generation of emGFP::Nup358 recombinant flies

The genomic Nup358 locus was tagged with the emeraldGFP CDS (GFP::Nup358) by homologous recombination mediated knock-in as described in (Gáspár et al., 2016). A double strand break was introduced 15 nt downstream of the ATG start codon by injecting a pU6-BbsI-chiRNA vector (Gratz et al., 2013) (Addgene, 45946) carrying a complementary guide RNA (5'-gTTTACAACGCGAAAAGAAGTGG-3' [see Key Resource Table for primers]) designed via the flyCRISPR Target Finder tool (http://flycrispr.molbio.wisc.edu) into *w[1118]; PBac{y[+mDint2] = vas-Cas9}VK00027* flies (BL-51324) (Norrander et al., 1983). Homologous recombination was mediated by co-injection of a template plasmid pAS095 (pUC19 backbone) carrying a loxP-GMR-3P3-EGFP-tubulin3'UTR-loxP-emGFP cassette flanked by two ~600 bp long homology sequences 5' and 3' of the ATG start codon to produce an in frame emGFP-Nup358 fusion. The marker cassette was later removed by Cre-mediated recombination and stable GFP::Nup358 heterozygous flies were crossed to homozygosity. Both males and females were viable, fertile, and showed no obvious phenotypes.

Generation of *sqh-Kuk* transgenic flies

The transgenic construct was cloned into a pCasper4-modified vector, containing a minigene of spaghetti-squash (sqh) where the ORF was replaced by a EGFP-W GATEWAY cassette taken form UASt-GW vector of Terence Murphy (Carnegie Institute). LR recombination was performed between a p221-*kuk* entry clone containing the full ORF of kuk (CG5175) and this pC4-SqhP-GW destination vector, resulting in the expression vector pC4-SqhP-EGFP::Kuk. Transgenesis was done according to standard procedures in *yw* flies and F2 transgenes were identified by eye color.

QUANTIFICATION AND STATISTICAL ANALYSIS

Image analysis

Fluorescence Intensity measurements, generation of kymographs and temporal projections were carried out in Fiji (Schindelin et al., 2012) with indicated plugins. To evaluate AL evolution in egg chambers (Figure 1G) integrated RFP::Nup107 intensities in either oocytes or nurse cells were measured from fixed egg chambers on maximum intensity projected stacks covering 5 μm. Statistical details can be found in corresponding Figure Legend. To quantify the temporal evolution of granules and AL during oogenesis (Figure 2H), GFP::Nup358 expressing egg chambers were dissected, fixed and stained with WGA-Alexa647 to label FG-Nups. For all stages, bright spheric Nup358 foci with no or little WGA staining were counted as Nup358 granules, WGA only foci as oocyte specific granules and double labeled amorphic foci as AL. For early (stages 5-7) and mid (stages 8-11) oogenesis granules were counted in nurse cells and oocytes respectively. In late oogenesis, nurse cells are lacking and only the oocyte was considered. Statistical details can be found in corresponding Figure Legend.

smFISH odd/even validation

To validate smFISH probe sets (representative example for *nup358* in Figure S4B), each set was split into non-overlapping odd and even numbered probes and labeled with Atto 633 and Atto 565 respectively. Hybridization and imaging was performed with both partial probe sets on the same sample. Acquired confocal volumes with a z step size of 0.18 μm were first deconvolved using the Huygens Essential software package. Automatic particle picking was performed using the _xsPT FIJI plugin (Gaspar et al., 2017; Gáspár et al., 2018) that identifies particles based on 2D Gaussian fitting and intensity thresholding. These particles are then tracked

in at least three consecutive z-slices based on their geometric center. 3D objects that fulfilled this criterion were recorded and plotted in R using Rstudio (https://www.rstudio.com/) and the ggplot2 library (Wickham, 2009). For every identified 3D particle in the reference channel, its intensity was plotted against the corresponding intensity in the target channel, which displays a linear correlation for probe sets targeting identical transcripts.

smFISH enrichment scores

For quantification of mRNA enrichment around Nup granules and the NE (Figure 5D), images were first deconvolved using the Huygens Essential software package. Datasets were processed separately for nurse cells and oocyte areas. Four slices (z = 0.72 μm) containing GFP::Nup107 positive structures were z-projected with maximum intensity. The GFP channel was then subjected to thresholding and manual particle selection. The corresponding selection was dilated by 0.4 μm and used to measure the corresponding average smFISH fluorescence intensity within the area. In the case of nuclear envelope enrichment, the area was only dilated toward the cytoplasm, since mRNA enrichment was restricted to the cytoplasmic side of the NE. The selection was subsequently inversed, non-cytoplasmic regions (e.g., nucleus, follicle cells) were excluded, and the average smFISH intensity of non-GFP::Nup107 associated signal was measured. The fold enrichment of each transcript was then calculated by dividing the average smFISH intensity corresponding to Nup107-positive structures by the remaining cytosolic average intensity. For the ribosome runoff assay (Figures S4I-S4I''), enrichment was further normalized to value at t = 0 min to represent the fraction remaining over time.

Quantification of shRNA-mediated depletion

To assess shRNA-mediated knockdown efficiency (Figures S3D and S6G), acquired confocal volumes with a z step size of 0.18 μm were first pre-processed by Gaussian blurring ($\sigma = 2$) to enhance semi-automated particle picking. Individual fluorescent spots were detected using the _xsPT FIJI plugin as described above. The identified single mRNA molecules were counted and normalized to a volume of 1,000 μm^3. mRNA concentrations for individual egg chambers were plotted for targeted (*nup358*, *embargoed*) and control (*white*) shRNA. Knockdown efficiencies were calculated by dividing respective mean concentrations in nurse cells and oocytes respectively. For *nup358*, RNAs tended to cluster in larger structures below the resolution limit of the confocal microscope. To circumvent this limitation, the intensity distribution in targeted and control egg chambers were fitted by multiple Gaussian functions in R using Rstudio and the mixtools package (https://cran.r-project.org/web/packages/mixtools/) Benaglia et al., (2009) as described previously (Gaspar et al., 2017). Each identified particle was then calibrated to the first Gaussian peak to estimate the copy number, which were used for visualization and calculation of knockdown efficiency as described above. Statistical details can be found in corresponding Figure Legend.

Intensity line profile measurements

For Figures S6C-S6E', a single confocal slice covering the nurse cell to oocyte border was acquired and the intensity of GFP::Nup358, anti-RanGAP immunofluorescence and RFP::Nup107 was measured along a line in FIJI averaging 10 pixels and plotted along its distance.

For Figure S5, a single representative confocal slice for each odd/even split probe set was analyzed by summation of Atto 565 and Atto 633 channel raw fluorescence intensities, followed by 18 pixel average intensity line profiles from anterior (nurse cells) to posterior (oocyte) in FIJI. The resultant intensity profiles were plotted along the distance, centered around the nurse cell – oocyte border. Lines were chosen at roughly the same z-depth and, wherever possible, to traverse one nurse cell nucleus. Dyes, microscope settings, as well as analysis parameters were kept constant in-between probe sets; however, intensities were not corrected for background fluorescence, degree of labeling, or number of available probes and might therefore vary between sets. A full list of probes used in this study is available in the attached spreadsheet (Table S1).

Quantification of Nup358 granules

To quantify Nup358 granule volumes under ectopic expression of different Ran mutants (Figure 6C), acquired confocal volumes with a z step size of 1 μm were used to train a machine learning segmentation model using the Pixel classification workflow in Ilastik (v1.3.2) (Sommer et al., 2011). The model was trained to recognize and segment GFP::Nup358 containing cytosolic granules but to exclude oocytic, nurse cell and follicle cell nuclei. Training was performed on a single *mat-Gal4; GFP::Nup358 / UAS-HA::RanQ69L* stage 10 egg chamber and then applied to all remaining stage 9 - 11 egg chambers of all genotypes in batch mode. The quality of segmentation was assessed by comparison with manual segmentation of a representative volume. Identified objects were then further processed in FIJI. First, the semantic segmentation was transformed into instance segmentation using 'Connected Component Labeling' in the MorphoLibJ plugin (Legland et al., 2016). The number and volume of all identified objects within a certain volume in each nurse cell compartment was then measured using the 'Analyze Regions 3D' command in the same plugin. The resultant integrated volume of all granules was divided by the total cytosolic volume and plotted as granule volume fraction (% v/v) for Ran, RanT24N and RanQ69L respectively. Statistical details can be found in corresponding Figure Legend.

Quantification after colchicine treatment

Ovaries were dissected from GFP::Nup358, RFP::Nup107 expressing females that have been subjected to Colchicine as described above. Confocal z stacks were acquired from living isolated egg chambers. From these images the fraction of double labeled AL and

non-overlapping GFP::Nup358 or RFP::Nup107 granules relative to the total number of granules plus AL were determined using FIJI. To account for different image sizes, numbers were normalized to 1,000 μm^2. Statistical details can be found in corresponding Figure Legend.

Quantification of granules upon *nup358* depletion

Control or nup358 shRNA induced ovaries from GFP::Nup358 expressing flies were dissected, fixed and stained with WGA to label FG-Nups, and subsequently imaged on a confocal microscope. WGA negative Nup358 granules in nurse cells and double labeled AL in oocytes were counted from recorded z stacks using FIJI. To compare between individuals, the amount of granules and AL respectively was normalized to 1,000 μm^2. Statistical details can be found in corresponding Figure Legend.

DATA AND CODE AVAILABILITY

Data including all imaging datasets produced in this study will be made available upon request.

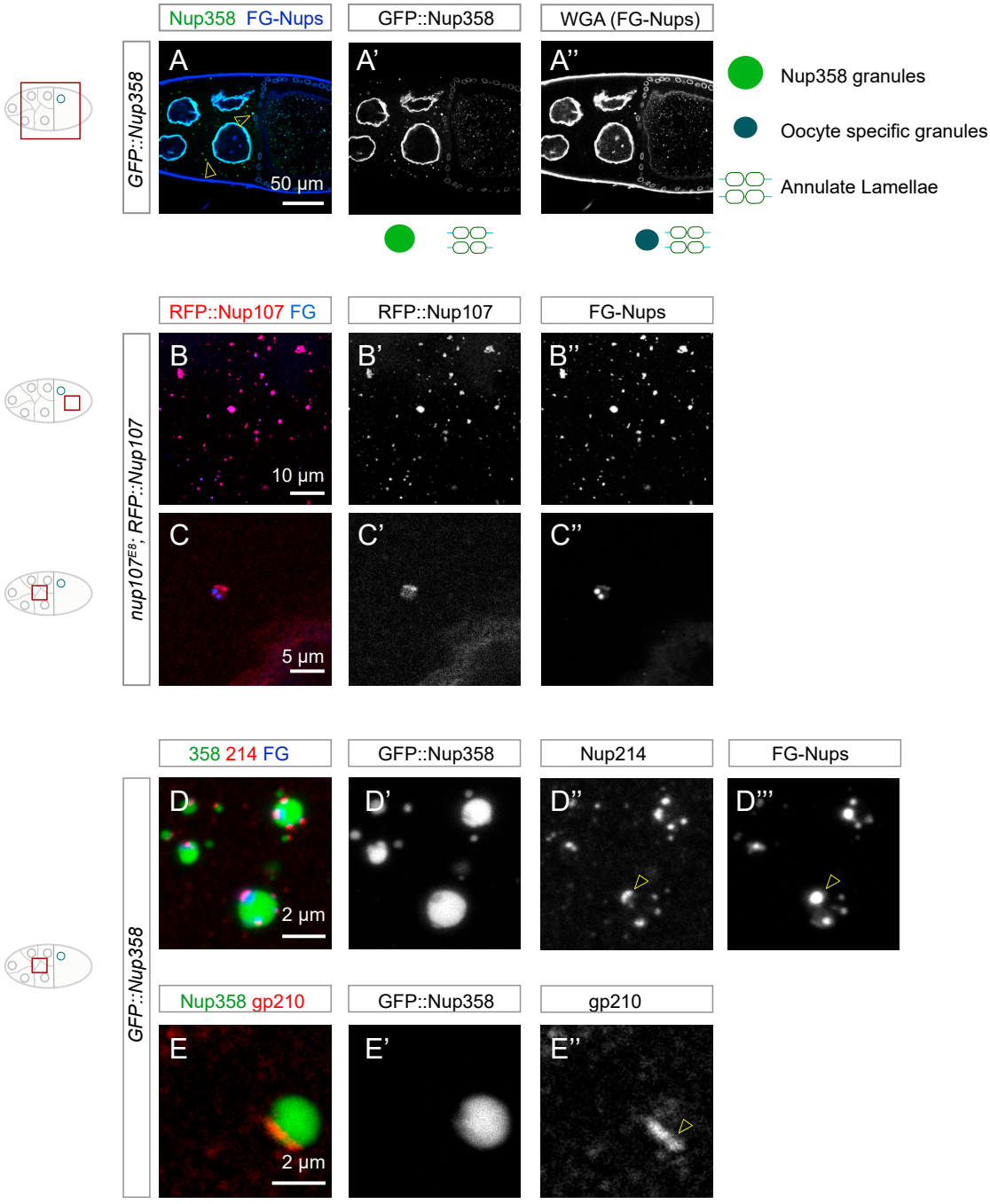

Figure S1. Nups Form Compositionally Diverse Granules, Related to Figure 2

(A) Classes of Nup granules. (A-A'') Top view confocal images of a fixed GFP::Nup358 expressing egg chamber stained for WGA-Alexa647, labeling FG-Nups. GFP::Nup358 and WGA colocalize at the NE of nurse and follicle cells and at AL in the ooplasm (A). In addition, GFP::Nup358 localizes to bright spherical Nup358 granules that are prevalent in nurse cells (yellow arrowheads in A). In the ooplasm, WGA stains dual labeled AL and oocyte specific granules that do not contain GFP::Nup358.

(B and C) Granules are not due to overexpression of Nup107. Top view confocal images of fixed egg chambers where RFP::Nup107 rescues the null allele *nup107*^{E8}. In the absence of endogenous Nup107, RFP::Nup107 condenses into oocyte specific granules and localizes to AL (B-B''). RFP::Nup107 condensation in nurse cells is rare (C-C'') and might be confined into Nup358 granules as exemplified in Figure 4A and 4C.

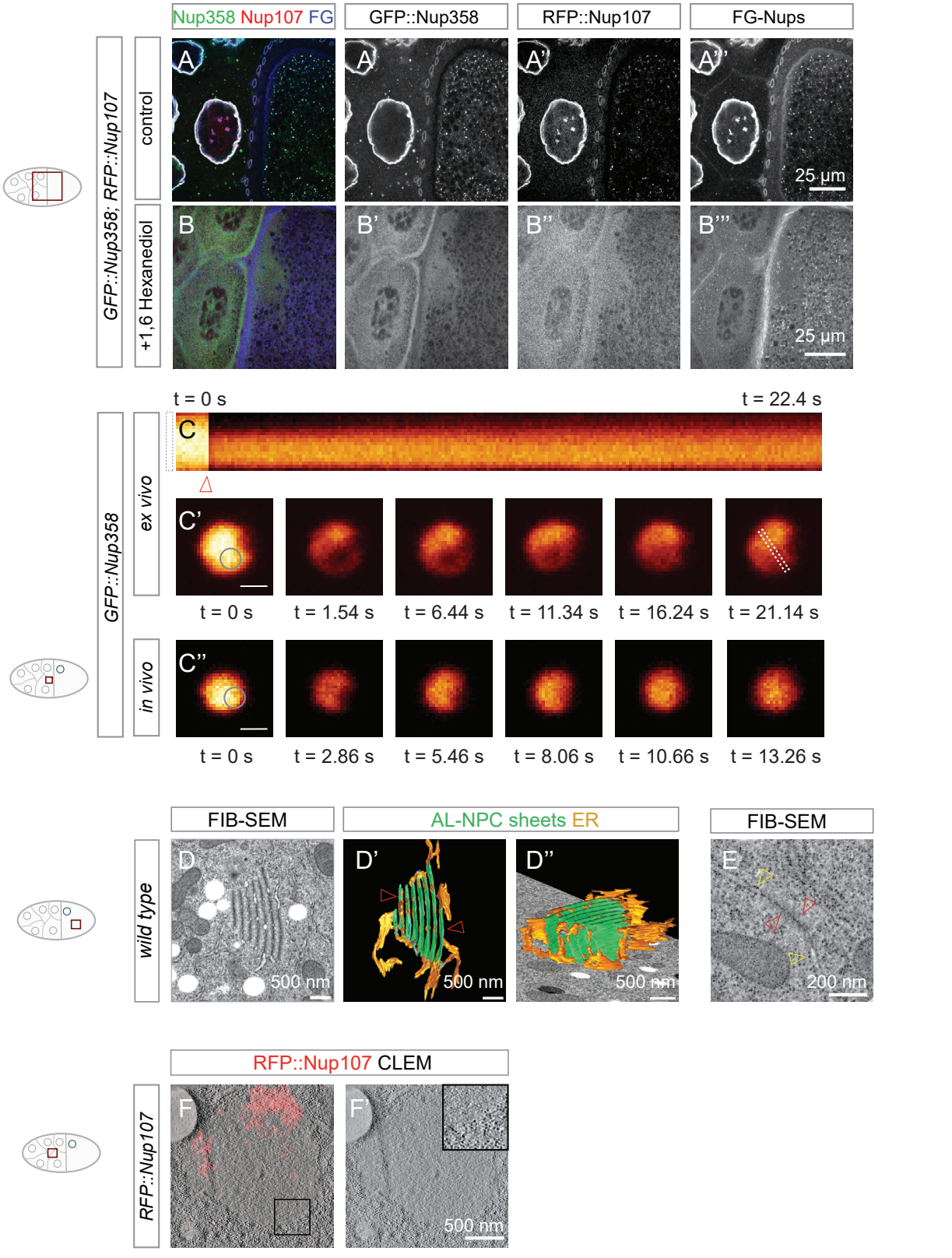

(legend on next page)

Figure S2. Nup Granules Fulfill Hallmarks of Biomolecular Condensates, Related to Figure 4

(A–C) NPCs and NPC precursor granules have properties of phase separated condensates. (A-B''') Top view images from fixed stage 10 egg chambers expressing GFP::Nup358 and RFP::Nup107, either incubated in S2 medium (A-A''') or S2 medium supplemented with 5% 1,6 Hexanediol (B-B''') for 10 min prior to fixation. FG-Nups were stained with WGA-Alexa647. NPCs and precursor granules disperse as indicated by the relocalization of GFP::Nup358 (B, B'), RFP::Nup107 (B, B'') and FG-Nups (B. B''') to the cytoplasm. (C-C''') Nup358 granules recover their fluorescence internally on short time scales. Kymograph (C) and single top view confocal stills (C', C'') of a time lapse video recording a photo-bleached GFP::Nup358 granule in a squashed ex vivo preparation (C, C') or in the intact nurse cell cytoplasm (C''). The round photo-bleached region in the granule is indicated by a circle in C' and C'', the ROI spanning the kymograph is indicated in the rightmost still in (C'). The arrowhead in (C) indicates the bleach pulse. Scalebar in (C', C'') is 1 μm.

(D and E) AL maintain characteristics of condensates. Single slices (D and E) and isosurface rendering (D', D'') of a FIB-SEM volume obtained in the oocyte. (D-D'') Multi-sheet AL have a complex membrane topology resulting in a partially open architecture exposed to the surrounding ooplasm (arrowheads in (D')), yet they retain a different milieu as indicated by the exclusion of ribosomes (Figure 4F'). (E) Even at a single sheet with AL-NPCs, ribosomes are excluded proximal to the NPCs (red arrowheads), while they directly contact membranes in the neighboring ER (yellow arrowheads).

(F) Condensation of Nup358 granules is not a consequence of the GFP tag. CLEM (F) and TEM (F') images of a RFP::Nup358 expressing egg chamber subjected to high pressure freezing, without GFP::Nup358. Ribosomes are excluded from a sphere that contains limited amounts of RFP::Nup107 at associated membranes, resembling a Nup358 granule. The condensate border is highlighted in the inset in (F'). See also Video S6.

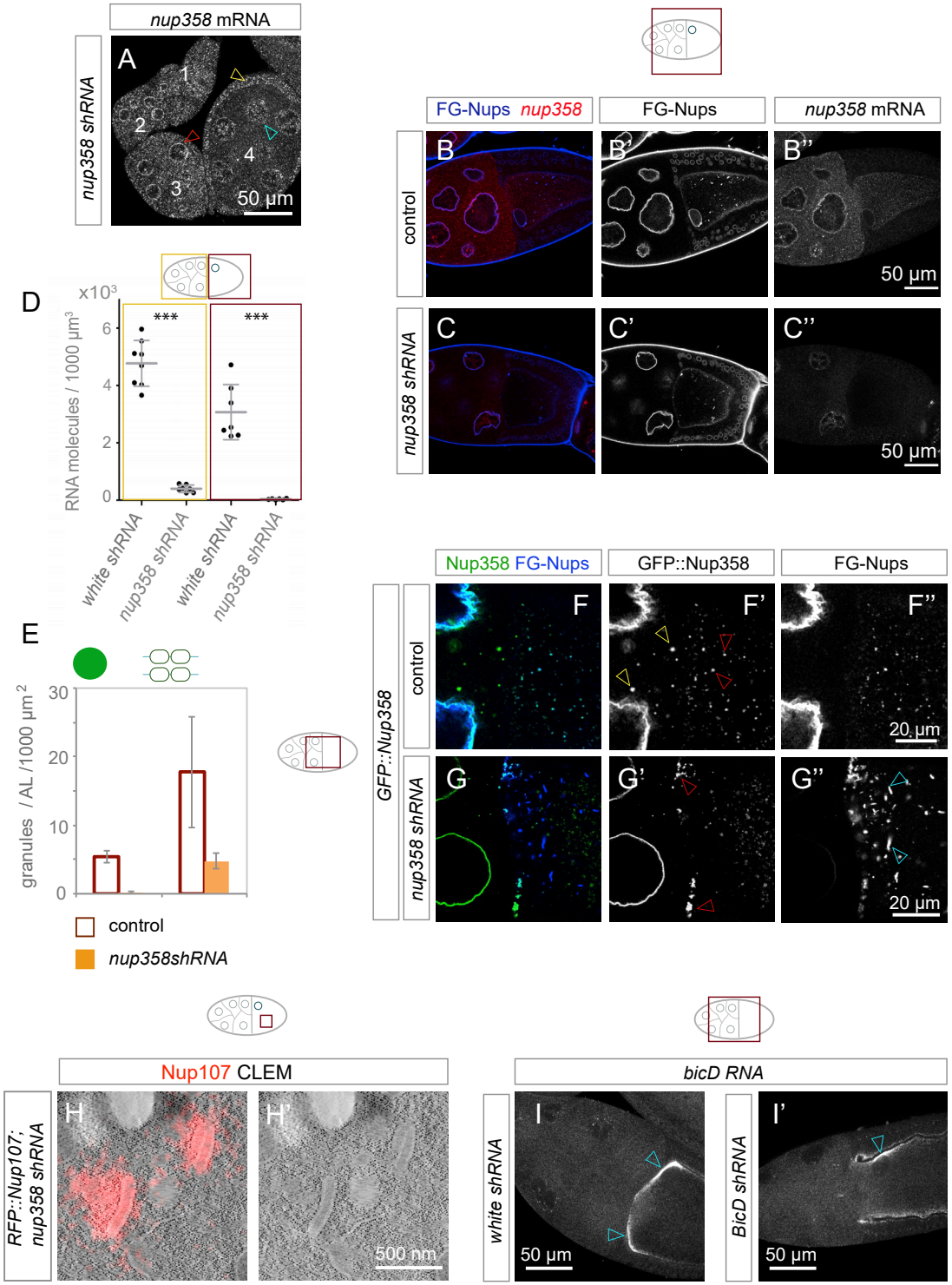

Figure S3. Nup358 Condensates Are Required for AL-NPC Biogenesis, Related to Figure 4

(A–D) Nup358 depletion during oogenesis. (A) Time dependency of shRNA induced depletion of *nup358* transcripts. Top view of a fixed chain of egg chambers, hybridized with smFISH probes detecting *nup358* mRNA. The image comprises four stages of development; numbers refer to stages, whereby 1 is the earliest. *Nup358* mRNA is still enriched at the NE of egg chamber 3 (red arrowhead), but is lost at stage 4 (cyan arrowhead). At stage 4, general levels of *nup358* mRNA have decreased, but not in follicle cells (yellow arrowhead), which are not affected by the germline-specific induction of *nup358* shRNA. (B and C) Top views of a fixed stage 10 egg chamber dissected from control (B-B'') or *nup358* depleted (C-C'') ovaries, stained with WGA-Alexa647, labeling FG-Nups (B, C, B', C') and stained with smFISH probes detecting *nup358* mRNA (B, B'', C, C''). At this stage of oogenesis, nup358 mRNA levels are strongly decreased in ovaries subjected

(legend continued on next page)

to shRNA (C, C'') compared to controls (B, B''). (D) Quantification of the *nup358 shRNA* induced knockdown (n = 7 volumes from 4 egg chambers for nurse cells and 6 volumes from 4 egg chambers for oocytes) based on smFISH molecule counting compared to control (*white* shRNA) egg chambers (n = 6 volumes from 3 egg chambers). In nurse cells, knockdown efficiency is 91.5%, in oocytes 98.8% (*** $p < 0.0001$, unpaired t test). Bars represent mean ± STDV.

(E) Nup358 is required to assemble AL. Quantification of Nup358 granules and AL in fixed control (n = 5) or *nup358 shRNA* treated (n = 4) egg chambers expressing GFP::Nup358 stained with WGA-Alexa647. Counted were round GFP::Nup358 condensates in nurse cells and double labeled structures in the ooplasm as AL. GFP::Nup358 negative WGA labeled structures were not registered as AL. Nup358 depletion abolishes condensation of the GFP::Nup358 in nurse cells and impairs AL assembly in the oocyte. Data represent means ± STDV.

(F and G) Nup358 is required for AL integrity and coalescence. Top view stills of a living control (F-F'') or *nup358 shRNA* induced (G-G'') egg chamber from flies expressing GFP::Nup358. WGA-Alexa 647 was injected to label FG-Nups. In control egg chambers, GFP::Nup358 condenses (yellow arrowheads in F') and colocalizes with FG-Nups at AL (F, red arrowheads in F'). In *nup358 shRNA* induced egg chambers, round Nup358 condensates disappear (G, G'). AL clustered at the anterior oocyte, when residual GFP:Nup358 is present (red arrowheads in G'). FG-Nup positive but GFP::Nup358 negative patches fail to coalesce but appear elongated (cyan arrowheads in G''). Note that images in (G, G') were recorded with elevated laser power to visualize residual GFP::Nup358.

(H) Nup358 is required for AL integrity. (H, H') CLEM experiment showing RFP::Nup107 fluorescence in a *nup358* depleted egg chamber. RFP::Nup107 labels a NPC free ER membrane proximal area. The ribosome-excluding halo is partially compromised and ribosomes decorate the membranes that are directly proximate to the surrounding ooplasm.

(I) *BicD* shRNA displays phenotypes resembling *BicD* mutants. In *BicD* shRNA induced egg chambers, *BicD* mRNA fails to accumulate along the anterior cortex as in controls (arrowheads in (I)), but localizes laterally (arrowhead in (I')). Oocyte growth and morphology are compromised (I') as well as nuclear positioning (see also Figure 4H).

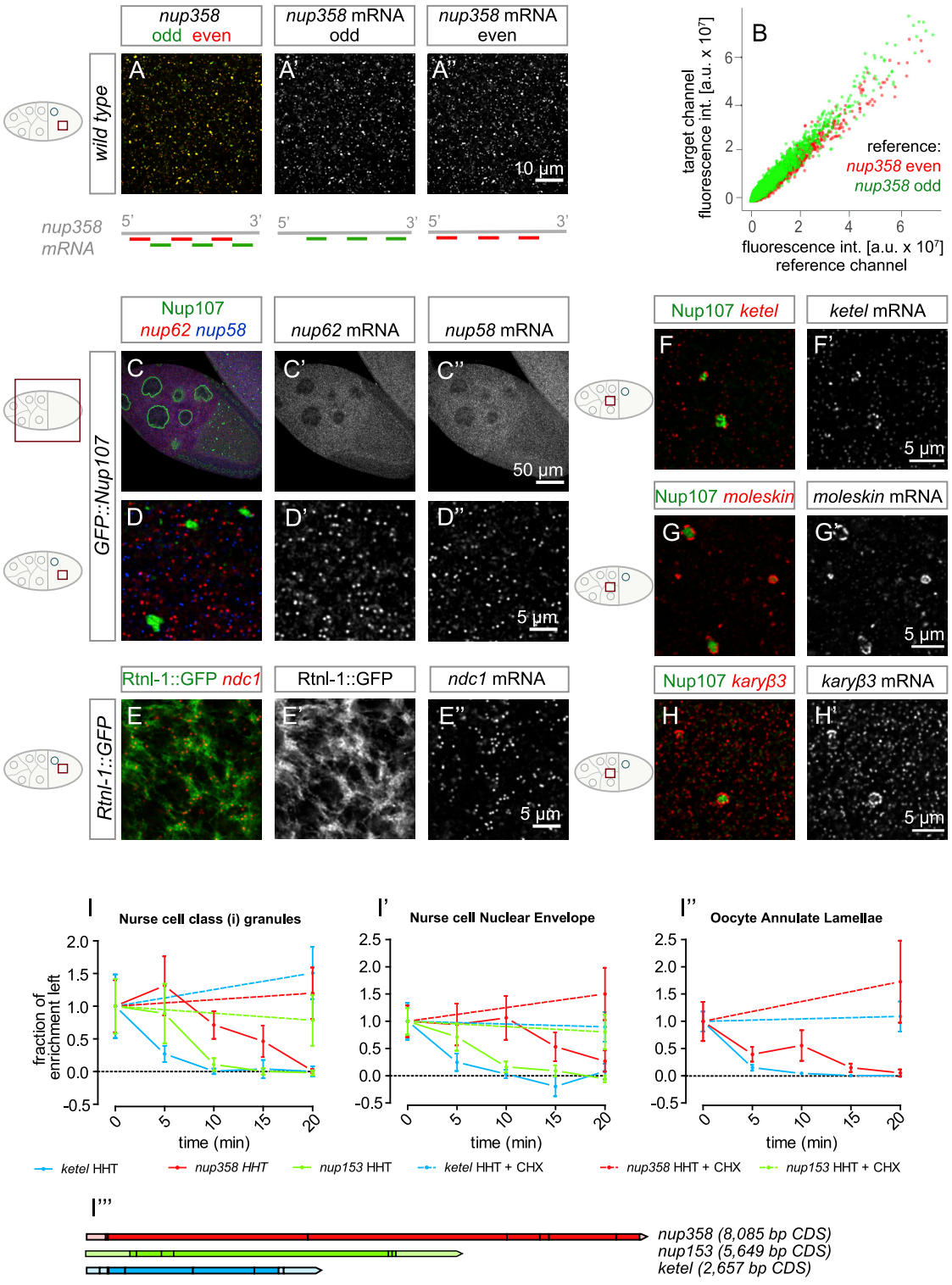

Figure S4. Specific NTR and Nup mRNAs Enrich at Germline NPC Assembly Sites, Related to Figure 5

(A) *nup358* smFISH probe co-localization validation. Representative confocal images of a stage 10 egg chamber hybridized with a *nup358* probe set that was split into odd (A') and even (A'') numbered probes (two independent sets of probes targeting alternating 19-21 nt long sequences within the ORF) labeled with Atto 633 or Atto 565, respectively. Signals from both channels co-localize to a high degree within the resolution and detection limits.

(legend continued on next page)

(B) Quantification of *nup358* odd and even probe co-localization. Automatic detection of smFISH particles in reference channel followed by raw intensity measurement in both channels. Each identified particle in the reference channel was plotted as a function of its corresponding fluorescence intensity in the target channel, displaying a linear correlation. a.u.: arbitrary units.

(C–E) Example localizations of several selected *nup* mRNAs. Low (C-C'') and high magnification (D-D'') confocal images of smFISH hybridization with *nup62* (Atto 633) and *nup58* (Atto 565) targeting probe sets imaged in a *GFP::Nup107* stage 10 egg chamber without significant co-localization. (E-E'') High magnification confocal images of *ndc1* (Atto 565) localization to ER in a stage 11 egg chamber. Rtnl1::GFP is used as ER marker.

(F–H) Example localizations of NTR transcripts displaying subcellular localization. *ketel* (F-F'), *moleskin* (G-G'), and *karyopherin β 3* (H-H') decorate the periphery of Nup358 granules.

(I) Ribosome run-off assays show length-dependent loss of RNA localization. Inhibition of translation initiation by incubation with homoharringtonine (HHT) in imaging medium for indicated amounts of time, followed by fixation, smFISH hybridization, confocal imaging and image quantification. Quantification of mRNA enrichment around Nup358 granules (I), NE (I') or AL (I'') relative to the average cytoplasmic intensity at different times after treatment, normalized to value at t = 0 min. *nup153* is absent in the oocyte AL measurement (I'') due to lack of enrichment (see Figure 5D). The remaining enrichment is displayed normalized to enrichment at 0 min and shows time-dependent loss of mRNA enrichment that corresponds to respective transcript length (I'''). Run-off is inhibited by additional incubation with translation elongation inhibitor cycloheximide (CHX) (I-I''). Circle and bars represent mean ± STDV. (I''') Schematic representing lengths of measured transcripts *nup358*, *nup153* and *ketel* drawn to scale.

A

	transcript	intensity line profile	comments
Cytoplasmic filaments	*nup358*		NE/AL
	nup214		homogenous
	aladin		homogenous
	mbo (nup88)		homogenous
Y-complex	*nup160*		homogenous, oocyte enriched early
	nup75 (nup85)		homogenous
	nup133		homogenous
	nup37		homogenous
	nup43		homogenous
	nup98-96		homogenous
	nup44a (seh1)		homogenous
	elys		homogenous
Inner ring	*nup93.1*		homogenous
	nup154 (nup155)		homogenous
	nup205		homogenous, slight NE enrichment
	nup35		homogenous
	nup188		homogenous
Central channel	*nup62*		homogenous
	nup54		homogenous
	nup58		homogenous
Nuclear basket	*mtor (tpr)*		granular, slight NE enrichment
	nup153		NE/AL
	nup50		homogenous, slight NE enrichment
TM nups	*ndc1*		ER
	gp210		slight NE, oocyte enriched early
Nuclear transport receptors	*ketel (importin β)*		NE/AL, oocyte enriched early
	karyopherin β3		NE/AL
	moleskin (importin 7)		NE/AL, oocyte enriched early
	importin β11		homogenous
	cadmus (importin 13)		homogenous
	transportin		homogenous
	transportin-SR		homogenous
	embargoed (crm1)		homogenous, oocyte enriched early
	karyopherin α1		homogenous, oocyte enriched early
	pendulin (karyopherin α2)		homogenous
	ntf2		homogenous
Ran cycle	*ran*		homogenous
	ranGAP		homogenous
	bj1 (rcc1)		homogenous, oocyte enriched early

B

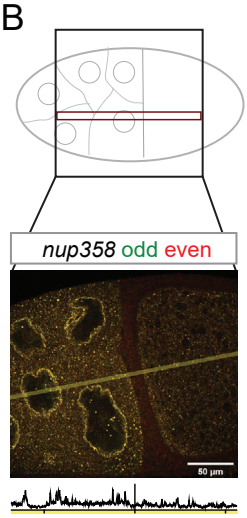

Figure S5. Overview of Nucleoporin and Related mRNA Localizations in *Drosophila* Egg Chambers, Related to Figure 5

(A–B) Overview of nup and related transcript distribution throughout the egg chamber. (A) Intensity line profiles (average over 18 pixels) throughout representative stage 10 egg chambers (centered at nurse cell – oocyte border) for each nucleoporin and –related mRNA targeting smFISH probe set. Each profile represents the

(legend continued on next page)

summed raw intensities of even and odd numbered probes labeled with Atto 565 and Atto 633 respectively and were imaged at constant microscope settings. The x axis displays the distance toward nurse cells (left) or oocyte (right) with 100 μm ticks. The y axis represents the summed raw intensity in A.U. from 0 to 130. The *moleskin* probe set was cut off at 130 for better overall visualization. Local minima occasionally occur if the line scan passes through a nucleus, as e.g., seen in *pendulin*, *ran*. (B) Cartoon representation of image analysis with example overlay of *nup358* even (red) / odd (green) smFISH probe set. The measurement area is highlighted with corresponding intensity line profile below.

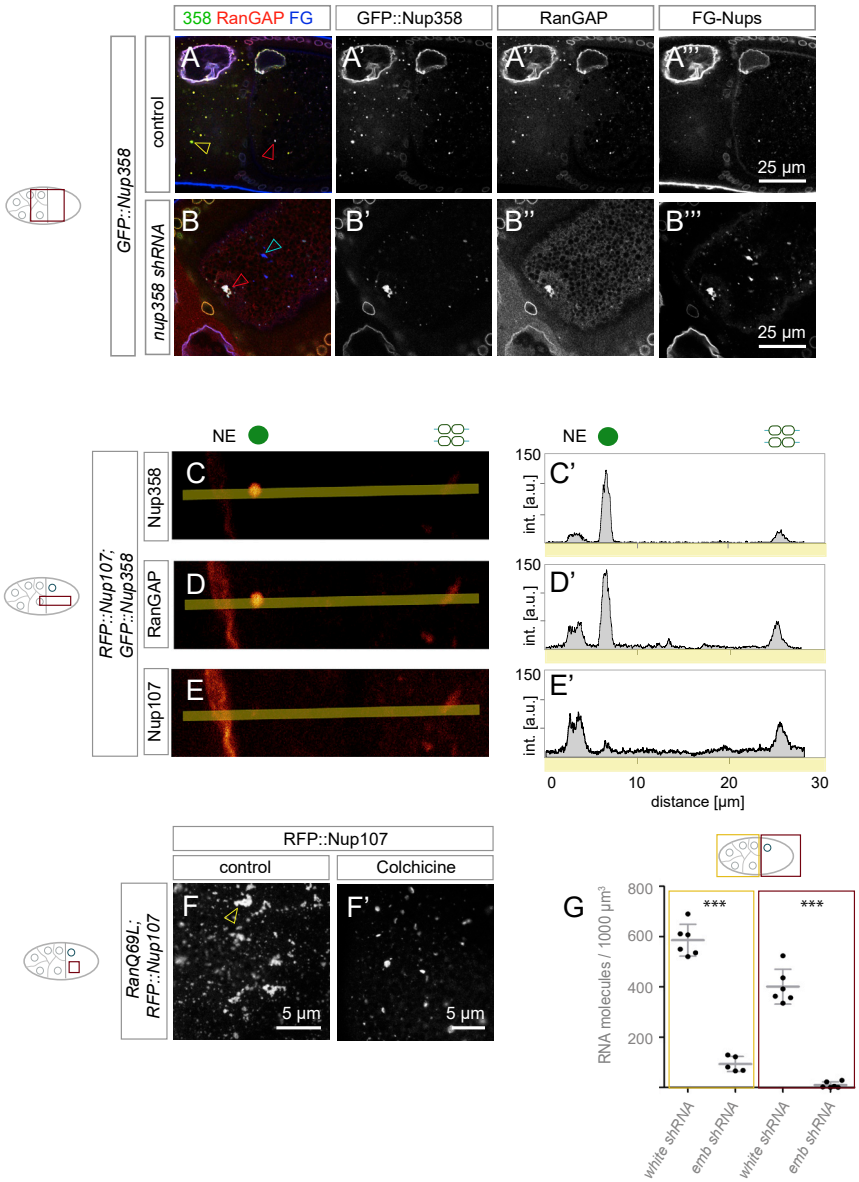

Figure S6. Ran and Crm1 Spatially Control Nup Condensation and AL Assembly, Related to Figure 6

(A and B) RanGAP localization to NPCs and Nup granules depends on Nup358. Top view images from either fixed control (A-A''') or *nup358* shRNA induced (B-B''') GFP::Nup358 expressing egg chambers, stained with an antibody detecting RanGAP and WGA-Alexa647, labeling FG-Nups. In control egg chambers RanGAP colocalizes with Nup358 at the NE, at Nup358 granules in nurse cells (yellow arrowhead in A) and to AL in the ooplasm (red arrowhead in A). (B-B') In *nup358 shRNA* induced egg chambers, Nup358 granules disappear (Figure S3E-G). Under these conditions, RanGAP largely relocalizes in the cytoplasm (B, B''). AL that preserve sufficient amounts of GFP::Nup358 maintain RanGAP (red arrowhead in B), yet they become larger. Granules without GFP::Nup358 lose RanGAP (cyan arrowhead in B). Note that panels in (B, B') were recorded with elevated laser power to visualize residual GFP::Nup358.

(C–E) Nup358 and RanGAP dilute upon progression into AL. Intensity differences in confocal images (C, D, and E) or corresponding intensity line profiles (10 pixel average) (C', D', E') of GFP::Nup358 (C and C'), anti RanGAP antibody staining (D and D') or RFP::Nup107 (E and E') at the NE, Nup358 granules or AL. GFP::Nup358 and RanGAP are enriched in Nup358 granules compared to AL, where RFP::Nup107 intensities are higher.

(F) RanGTP induced AL agglomeration depends on MTs. Top view stills of oocytes from movies taken from RanQ69L overexpressing flies that had been fed with (F') or without (F) colchicine. The AL agglomeration induced by RanQ69L (arrowhead in F) is suppressed by colchicine-induced de-polymerization of MTs (F').

(G) Quantification of the *embargoed shRNA* induced knockdown (n = 5 volumes for nurse cells and 6 volumes for oocytes from 3 egg chambers) based on smFISH molecule counting compared to control (*white* shRNA) egg chambers (n = 6 volumes from 3 egg chambers). In nurse cells, knockdown efficiency is 94.2%, in oocytes 97.7% (*** $p < 0.0001$, unpaired t test). Bars represent mean ± STDV.